




Deletion of ferroportin in murine myeloid cells increases iron accumulation and stimulates osteoclastogenesis *in vitro* and *in vivo*

Received for publication, November 6, 2017, and in revised form, May 1, 2018. Published, Papers in Press, May 3, 2018, DOI 10.1074/jbc.RA117.000834

Lei Wang^{‡§1}, Bin Fang^{§¶1}, Toshifumi Fujiwara^{§1}, Kimberly Krager^{||2}, Akshita Gorantla^{||}, Chaoyuan Li^{**}, Jian Q. Feng^{**}, Michael L. Jennings^{‡¶}, Jian Zhou^{‡3},  Nukhet Aykin-Burns^{||2,4}, and Haibo Zhao^{§¶§§¶¶5}

From the [‡]Department of Orthopedics, First Affiliated Hospital, Anhui Medical University, Hefei, Anhui 230022, China, the [§]Center for Osteoporosis and Metabolic Bone Diseases, Division of Endocrinology and Metabolism, Department of Internal Medicine, ^{||}Division of Radiation Health, Department of Pharmaceutical Sciences, and ^{¶¶}Department of Physiology and Biophysics, University of Arkansas for Medical Sciences, Little Rock, Arkansas 72205, the [¶]Department of Hematology, Union Hospital, Tongji Medical College, Huazhong University of Science and Technology, Wuhan, Hubei 430022, China, the ^{**}Department of Biomedical Sciences, Texas A&M College of Dentistry, Dallas, Texas 75246, the ^{§§}Research Department, Tibor Rubin Veterans Affairs Medical Center, Veterans Affairs Long Beach Healthcare System, Long Beach, California 90822, and the ^{¶¶}Division of Endocrinology, Department of Medicine, University of California at Irvine, Irvine, California 92697

Edited by Amanda J. Fosang

Osteoporosis, osteopenia, and pathological bone fractures are frequent complications of iron-overload conditions such as hereditary hemochromatosis, thalassemia, and sickle cell disease. Moreover, animal models of iron overload have revealed increased bone resorption and decreased bone formation. Although systemic iron overload affects multiple organs and tissues, leading to significant changes on bone modeling and remodeling, the cell autonomous effects of excessive iron on bone cells remain unknown. Here, to elucidate the role of cellular iron homeostasis in osteoclasts, we generated two mouse strains in which solute carrier family 40 member 1 (*Slc40a1*), a gene encoding ferroportin (FPN), the sole iron exporter in mammalian cells, was specifically deleted in myeloid osteoclast precursors or mature cells. The FPN deletion mildly increased iron levels in both precursor and mature osteoclasts, and its loss in precursors, but not in mature cells, increased osteoclastogenesis and decreased bone mass *in vivo*. Of note, these phenotypes were more pronounced in female than in male mice. *In vitro* studies revealed that the elevated intracellular iron promoted macrophage proliferation and amplified expression of nuclear factor of activated T cells 1 (*Nfatc1*) and PPAR γ coactivator 1 β (*Pgc-1 β*), two transcription factors critical for osteoclast differentiation. However, the iron excess did not affect osteoclast sur-

vival. While increased iron stimulated global mitochondrial metabolism in osteoclast precursors, it had little influence on mitochondrial mass and reactive oxygen species production. These results indicate that FPN-regulated intracellular iron levels are critical for mitochondrial metabolism, osteoclastogenesis, and skeletal homeostasis in mice.

Bone resorption by osteoclasts and bone formation by osteoblasts play an essential role in skeletal development, homeostasis, and repair (1, 2). In adults, bone resorption is coupled and balanced by bone formation in a self-renewal process called bone remodeling. Through this process, bone mass and strength are constantly maintained (3, 4). In most metabolic bone diseases, such as postmenopausal osteoporosis, Paget's disease of bone, periodontal disease, and osteolytic metastasis of tumors, excessive bone resorption caused by either increased osteoclast number or enhanced activity leads to pathological bone loss (5). Thus, unfolding the cellular and molecular mechanisms of osteoclast differentiation and function under physiological and pathological conditions will not only advance our understanding of osteoclast biology but will lead to the development of novel therapies for treatment of bone loss in a variety of skeletal diseases.

Osteoclasts are multinucleated cells formed by fusion of mononuclear progenitors that are differentiated from the monocyte/macrophage lineage of hematopoietic stem cells. M-CSF⁶ and RANKL are two indispensable cytokines for oste-

This work was supported by Chinese Natural Science Fund Grant 81501843 (to J. Z.), National Institutes of Health Grants AR062012 and AR068509 from NIAMS (to H. Z.), University of Arkansas for Medical Sciences (UAMS) Bridge Fund, UAMS Medical Research Endowment Award (to H. Z.), and by National Institutes of Health Grant R01 DE025659 (to J. Q. F.). The authors declare that they have no conflicts of interest with the contents of this article. The content is solely the responsibility of the authors and does not necessarily represent the official views of the National Institutes of Health.

¹ These authors contributed equally to this work.

² Supported by National Institutes of Health Grant GM109005 from NIGMS and Grant ES022781 from NIEHS.

³ To whom correspondence may be addressed. Tel.: 86-0551-6292-3771; Fax: 86-0551-363-3742; E-mail: zhoujian831207@163.com.

⁴ To whom correspondence may be addressed. Tel.: 501-603-1375; Fax: 501-526-6510; E-mail: NAykinburns@uams.edu.

⁵ To whom correspondence may be addressed. Tel.: 501-686-5130; Fax: 501-686-8148; E-mail: hzhao@uams.edu.

⁶ The abbreviations used are: M-CSF, macrophage colony-stimulating factor; 7'AAD, 7-aminoactinomycin-D; BMM, bone marrow monocyte; *Ctsk*-Cre, cathepsin K-Cre; DHE, dihydroethidium; ERK, extracellular signal-regulated kinase; FPN, ferroportin; *LysM*-Cre, lysozyme M-Cre; mtROS, mitochondrion-derived ROS; NOX, NADPH oxidase; OCR, oxygen-consumption rate; PGC1 β , peroxisome proliferator-activated receptor γ coactivator 1 β ; PI3K, phosphoinositide-3-kinase; PINP, the N-terminal propeptide of type I collagen; ROS, reactive oxygen species; Tf, transferrin; TRAcP, tartrate-resistant acid phosphatase; WGA, wheat germ agglutinin; MFI, mean fluorescence intensity; OC, osteoclast; pOC, pre-osteoclast; qPCR, quantitative PCR; RANKL, receptor activator of NF- κ B ligand; ANOVA, analysis of vari-

oclastogenesis *in vitro* and *in vivo*. Although M-CSF regulates the proliferation of macrophages and the survival of osteoclasts via activation of extracellular signal-regulated kinase (ERK) and phosphoinositide-3-kinase/Akt (PI3K/AKT) pathways (6, 7), RANKL is a major osteoclast differentiation factor. RANKL activates mitogen-activated protein kinase, NF- κ B, and PI3K/AKT pathways (8). With the assistance of costimulating signals derived from immunoglobulin-like receptors with immunoreceptor tyrosine-based activation motif and their associated adapter proteins, RANKL induces calcium oscillation. These pathways converge to induce and activate a transcription complex, including the nuclear factor of activated T cells 1 (NFATc1), a master transcription factor of osteoclast differentiation (9, 10).

Mitochondria are the major source of cellular ATP generated through the process of oxidative phosphorylation. Indeed, the high density of numerous mitochondria in osteoclasts was observed as early as the 1930s (11), which was confirmed by other early reports (12, 13). Recent studies using genetically modified mouse models have revealed that mitochondria and their transcriptional regulator PGC1 β (peroxisome proliferator-activated receptor γ coactivator 1 β) are crucial for osteoclast differentiation and function *in vivo* and *in vitro* (14–16). Despite these advances, the molecular mechanisms and pathways regulating the augmentation of mitochondrial biogenesis and metabolism during osteoclastogenesis remain largely unknown.

In addition to ATP, the mitochondrial respiratory chain reactions also generate reactive oxygen species (ROS) (17). Although aberrantly enhanced ROS cause DNA and protein damages and are harmful, there is growing evidence that ROS at the physiological level function as important regulators of intracellular signaling pathways (18, 19). Accordingly, it has been reported that ROS stimulate osteoclasts and are culprits of estrogen deficiency–induced bone loss (20, 21). Moreover, antioxidants attenuate osteoclastogenesis and prevent bone loss in ovariectomized mice (22–24). ROS promote osteoclast differentiation by enhancing RANKL-induced signaling pathways (25–27). ROS generated by NADPH oxidases (NOX), especially NOX4 (28, 29), and by mitochondria (mtROS) (30–32) seem play an important role in the regulation of osteoclasts.

Iron is an essential element for organismal homeostasis (33). It plays a fundamental role in mitochondrial metabolism and the biosynthesis of heme and Fe-S clusters, which are critical components of the mitochondrial respiratory complexes (34). As a transitional redox-active metal, cellular labile iron induces ROS production through the Fenton reaction (35). Mammalian cells acquire iron through uptake of transferrin, heme, ferritins, or via nontransferrin-bound iron import (36). Cellular iron that is not utilized is either stored in ferritin or is exported via ferroportin (FPN). FPN, encoded by the *Slc40a1* gene, is the only cellular iron exporter identified so far in mammalian cells (37). It plays an essential role in systemic iron homeostasis by medi-

ating intestinal iron absorption and by releasing iron from macrophage recycle and hepatic storage (38).

Mutations of the *Slc40a1* gene cause autosomal recessive or dominant forms of hemochromatosis, an iron-overload disorder (39–41). Whereas germline deletion of *Fpn* in mice leads to embryonic lethality, intestine-specific *Fpn* knockout mice develop anemia (42). Macrophage *Fpn*-deletion mice are relatively normal with a mild anemia and iron accumulation in macrophages (43). More recently, it has been shown that the mRNA expression of *Fpn* decreases during osteoclast differentiation and knocking down *Fpn in vitro* promotes myeloma-induced osteoclast differentiation and bone resorption (44).

Increased bone resorption and low bone mass are frequent complications of hemochromatosis, a hereditary iron overload disease, and thalassemia and sickle cell disease patients who often have transfusional iron overload (45–47). With the prolonged life span of these patients after iron chelation and transfusion therapies during the past decades, osteoporosis and subsequent bone fractures have become a major healthcare issue in management of these patients (48–50). Several clinical studies have reported that iron overload in these patients induces increased bone resorption (51, 52). Some studies indicate that impaired bone formation is involved (53). Moreover, iron overload in mice leads to increased bone resorption and oxidative stress that exacerbate estrogen-deficiency bone loss (54, 55). In contrast, iron chelation inhibits generation of osteoclasts *in vitro* and prevents bone loss in ovariectomized mice (14, 56). Iron functioning together with PGC1 β regulate mitochondrial biogenesis and promote osteoclast differentiation (14). Although these previous reports pinpoint an important role of iron metabolism in bone homeostasis, the cell autonomous effects of iron on mitochondrial biogenesis, energy metabolism, and ROS production in osteoclast lineage cells remain unknown. Understanding how systemic and cellular iron regulates bone cells and skeletal homeostasis will help develop novel therapies for iron overload bone diseases.

In this study, we set out to elucidate the role of cellular iron homeostasis in osteoclast differentiation and function using *Fpn* myeloid and mature osteoclast conditional knockout mouse models. The results reported here indicate that FPN-regulated intracellular iron levels are critical for mitochondrial respiration, osteoclastogenesis, and skeletal homeostasis in mice.

Results

Deletion of *Fpn* in osteoclast precursors but not in mature cells leads to increased osteoclastogenesis and declined bone mass in female mice

Although systemic iron deficiency and overload have significant impacts on skeletal health, the intrinsic effects of iron metabolism on bone cells remain largely unknown. To elucidate the role of cellular iron in osteoclast differentiation and function *in vivo* and *in vitro*, we crossed *Fpn*-floxed mice, in which exons 6 and 7 of the murine *Slc40a1* gene were flanked by two loxP sites (42), with lysozyme M-Cre (*LysM-Cre*) and cathepsin K-Cre (*Ctsk-Cre*) mice to generate conditional

ance; BrdU, bromodeoxyuridine; FCCP, carbonyl cyanide 4-(trifluoromethoxy)phenylhydrazone; ESI, electrospray ionization; ETC, electron transport chain; α -MEM, α -minimal essential medium; FSC, forward scatter; SSC, side scatter.

Ferroportin and osteoclast formation

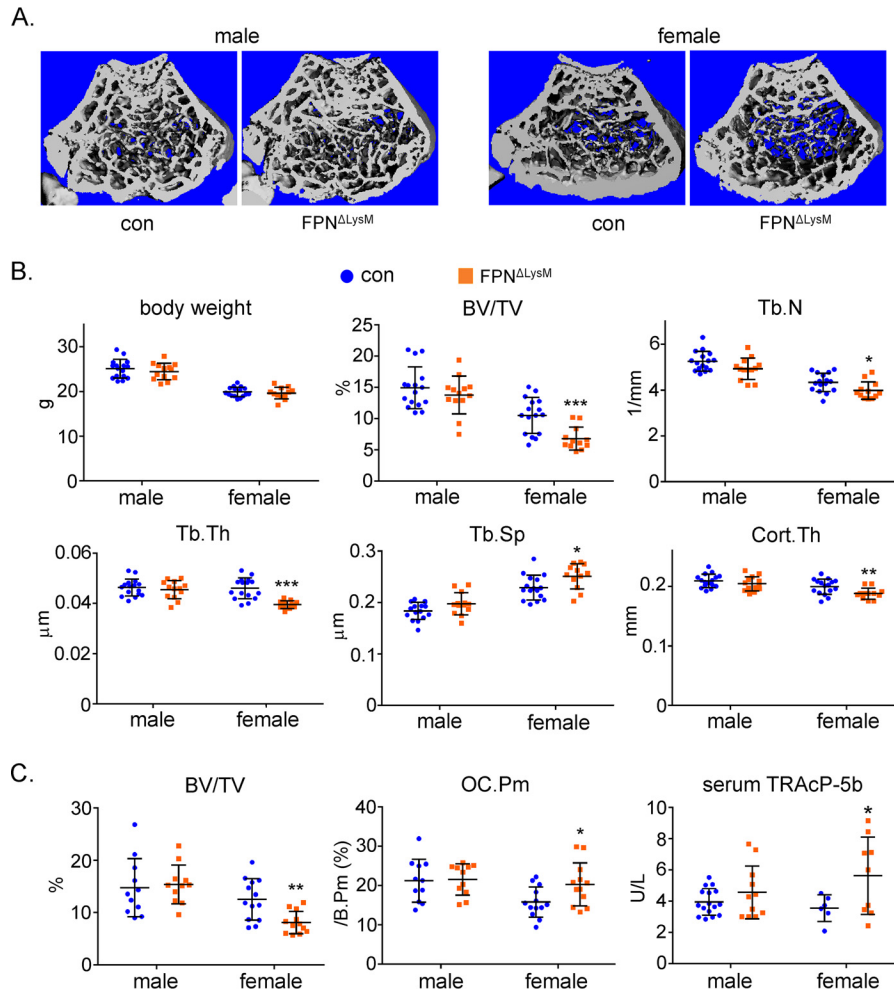


Figure 1. Conditional deletion of *Fpn* in osteoclast precursor cells results in decreased bone mass and increased osteoclasts in female mice. *A* and *B*, μ CT images and analyses of the trabecular and cortical bone compartments of the left femur of 2-month-old male and female control (*con*) and *Fpn* conditional deletion (*cKO*) mice (male control, $n = 16$, and *cKO*, $n = 13$; female control, $n = 16$, and *cKO*, $n = 12$). *C*, histomorphometry analyses of the paraffin-embedded TRAcP-stained tissue sections of the right femurs of control and *cKO* mice (male control, $n = 11$, and *cKO*, $n = 11$; female control, $n = 13$, and *cKO*, $n = 12$). The serum level of osteoclast-specific TRAcP-5b was measured by ELISA. *BV/TV*, percentage of trabecular bone volume to tissue volume; *Tb.N*, trabecular number; *Tb.Th*, trabecular thickness; *Tb.Sp*, trabecular separation; *Cort.Th*, cortical bone thickness of femur mid-shaft; *OC.Pm*, osteoclast perimeter. *, $p < 0.05$; **, $p < 0.01$; ***, $p < 0.001$ versus control by Student's *t* test.

knockout mouse strains with specific deletions of *Fpn* in myeloid osteoclast precursors and mature cells, respectively (57, 58). The *Fpn*-*flox/flox*;*LysM*-*Cre*/+ and *Fpn*-*flox/flox*;*CtsK*-*Cre*/+ mice in C57BL/6 and 129 mixed background were designated as myeloid (*Fpn* ^{Δ LysM}) and osteoclast (*Fpn* ^{Δ Ctsk}) *Fpn* knockout mice. The corresponding *Fpn*-+/+;*Cre*/+ littermates were used as controls.

Both *Fpn* ^{Δ LysM} and *Fpn* ^{Δ Ctsk} mice were viable and normal in size and body weight with no overt abnormalities (Figs. 1 and 2). In accordance with a previous report (43), both male and female *Fpn* ^{Δ LysM} mice exhibited a moderate iron accumulation as reflected by an increased serum level of iron storage protein ferritin, as compared with their littermate controls. The increase in serum ferritin was more pronounced in female as compared with male *Fpn* ^{Δ LysM} mice (Fig. S1). Micro-CT analysis of both long bones and vertebrae from 2-month-old mice demonstrated decreased trabecular bone mass that is associated with declined trabecular numbers, trabecular thickness, and increased trabecular separation in female but not in male *Fpn* ^{Δ LysM} mice compared with their littermate controls (Fig. 1,

A and *B* and Fig. S2). Histomorphometry analysis of paraffin-embedded, tartrate-resistant acid phosphatase (TRAcP)-stained sections of distal femurs revealed a similar reduction in trabecular bone volume with elevated osteoclast intensity in female *Fpn* ^{Δ LysM} mice (Fig. 1C). In support of this finding, the serum level of TRAcP-5b, an *in vivo* specific marker of osteoclast number and bone resorption (59), increased in female *Fpn* ^{Δ LysM} mice (Fig. 1C).

Specific deletion of *Fpn* in the late stage of differentiated osteoclasts by *Ctsk*-*Cre* (Fig. 2, *A* and *B*), however, had no obvious effects on both trabecular and cortical bone mass and structures in long bones and vertebrae (Fig. 2C and Fig. S3). In contrast to *Fpn* ^{Δ LysM} mice, *Fpn* ^{Δ Ctsk} mice exhibited the similar levels of systemic iron content to their littermate controls, revealed by serum ferritin measurement (Fig. S4A) and serum CTx-I, a global marker of bone resorption (Fig. S4B) (60). Loss of *Fpn* in osteoclast lineage cells in mice had no significant influence on osteoblastic bone formation as measured by serum PINP (the N-terminal propeptide of type I collagen), a global marker of bone formation (Fig. S5). These data indicate that the

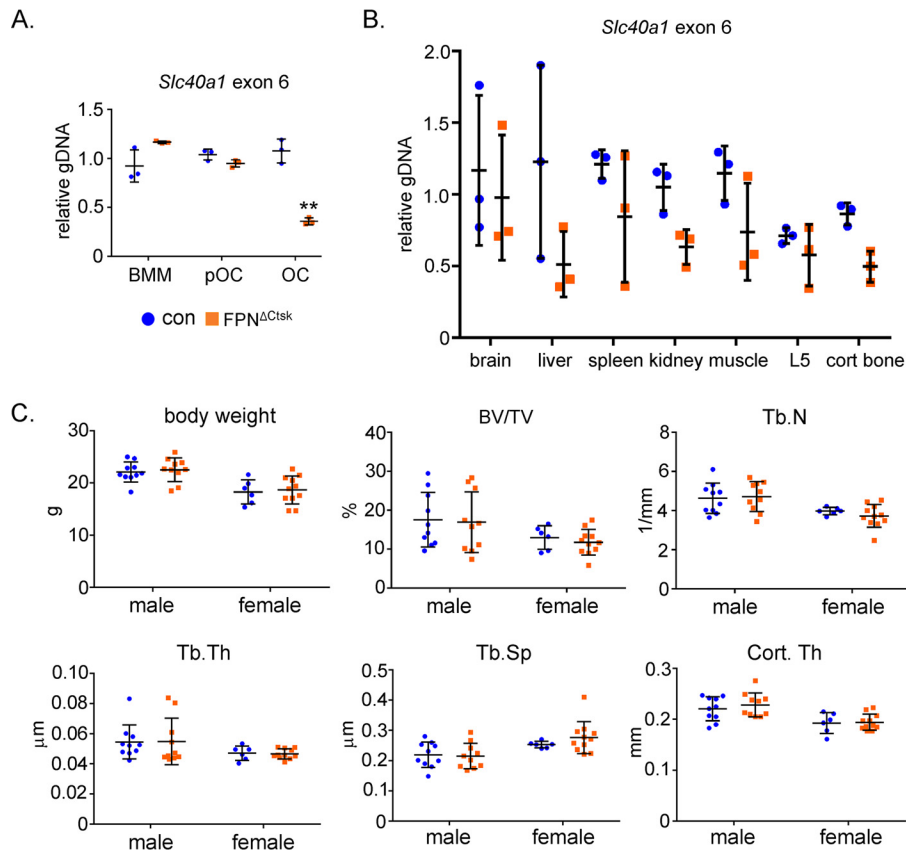


Figure 2. Loss of *Fpn* in late stage of osteoclast lineage cells has no effect on bone homeostasis in both male and female mice. *A*, quantitative real-time PCR detection of exon 6 of murine *Slc40a1* genomic DNA using genomic DNA isolated from control (*con*) and *Fpn* osteoclast-deletion (*Fpn*^{ΔCtsk}) cells during osteoclast differentiation. *n* = 3. *B*, quantitative real-time PCR detection of exon 6 of murine *Slc40a1* genomic DNA, normalized to a copy number control locus, using genomic DNA isolated from the indicated soft tissues, the L5 lumbar vertebra, and the tibia cortical bone compartment (*n* = 3). *C*, μ CT analyses of the trabecular and cortical bone compartments of the left femurs of 2-month-old male and female control (*con*) and *Fpn* conditional deletion (*cKO*) mice (male control, *n* = 10, and *cKO*, *n* = 10; female control, *n* = 6, and *cKO* *n* = 11). *BV/TV*, percentage of trabecular bone volume to tissue volume; *Tb. N*, trabecular number; *Tb. Th*, trabecular thickness; *Tb.Sp*, trabecular separation; *Cort. Th*, cortical bone thickness of femur mid-shaft. **, *p* < 0.01.

iron-regulator FPN plays an important role in bone remodeling by regulating osteoclastogenesis in mice.

***Fpn*-deficient osteoclast precursors have increased intracellular iron accumulation and exhibit accelerated osteoclast formation in vitro**

We first used real-time PCR to quantitatively detect the mRNA expression of *Fpn* in control and *Fpn*^{ΔLysM} osteoclast precursor and mature cells. As shown in Fig. 3A, the mRNA level of *Fpn* decreased dramatically during osteoclast differentiation in control cells. This finding is consistent with a recent report (44). The *Fpn* expression was significantly reduced in all *Fpn*^{ΔLysM} osteoclast lineage cells compared with control cells.

To determine how *Fpn* deletion affects cellular iron in osteoclast precursors, we conducted transferrin (Tf)-Fe⁵⁹ uptake assay in bone marrow monocytes (BMMs) derived from control and *Fpn*^{ΔLysM} mice. Consistent with a previous report (43), loss of *Fpn* led to an accumulation of Tf-Fe⁵⁹ in monocytes (Fig. 3B). The increased intracellular iron content in *Fpn*^{ΔLysM} osteoclast lineage cells was further confirmed by a colorimetric iron assay that detects the total iron (Fe²⁺ and Fe³⁺) (Fig. 3C).

Next, we set out to identify the effects of increased cellular iron on osteoclastogenesis *in vitro*. The control and *Fpn*-null BMMs were cultured with M-CSF and RANKL for 3 and 4 days

before fixation. The cells were then stained for TRAcP, an osteoclast differentiation marker. The total number of multinucleated TRAcP⁺ osteoclasts was counted. There was a significant increase in osteoclast formation in *Fpn*-depleting BMM cultures compared with controls (Fig. 3, D and E). A similar phenomenon was observed in BMMs cultured on cortical bovine bone slices (Fig. 3D, right panels). The accelerated osteoclastogenesis in *Fpn*-null BMMs was further confirmed by a higher mRNA expression of osteoclast marker genes, *Acp5* (encoding TRAcP), *Nfatc1* (encoding key osteoclast transcription factor Nfatc1), and *Ppargc1b* (encoding Pgc-1 β) in *Fpn*-null osteoclast lineage cells than in control ones (Fig. 3F). Similarly, loss of *Fpn* resulted in elevation of protein levels of CTSK, NFATc1, and PGC-1 β in the course of osteoclast differentiation (Fig. 3G). Taken together, these data indicate that loss of *Fpn* in osteoclast precursor cells leads to a moderate increase in cellular iron that promotes osteoclast differentiation.

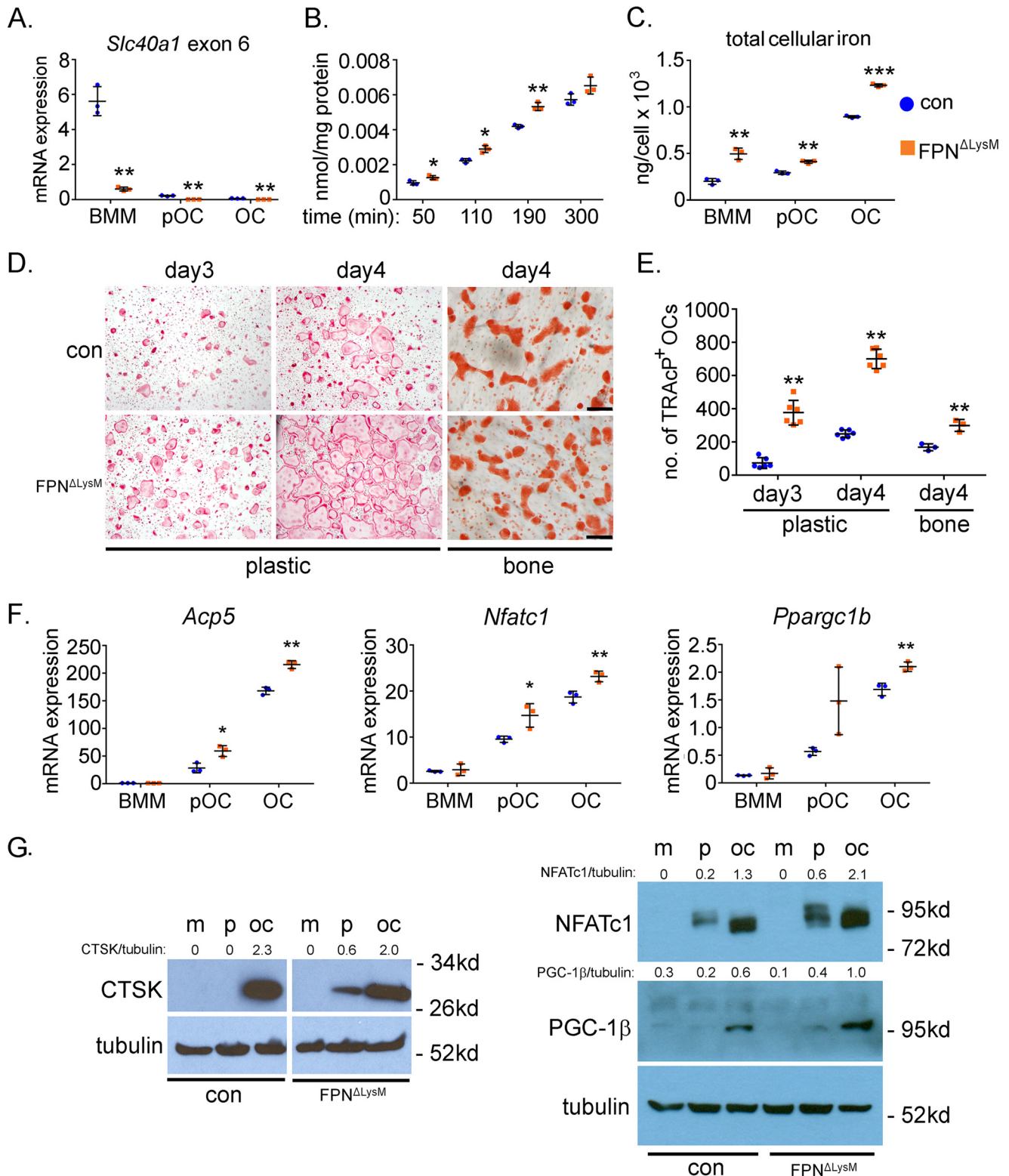
Increased intracellular iron in *Fpn*-null mature osteoclasts has no effect on osteoclastogenesis and bone resorption in vitro

To assess the role of FPN-regulated iron homeostasis in mature osteoclasts, we cultured bone marrow cells from control and *Fpn*^{ΔCtsk} mice with M-CSF plus RANKL for 4 days to generate mature osteoclasts. The result from the Tf-Fe⁵⁹

Ferroportin and osteoclast formation

uptake assay in mature osteoclasts demonstrated that there was a slight but significant increase in *Fpn*-null osteoclasts relative to control cells (Fig. 4A). When the intracellular total iron was measured by a colorimetric iron assay, however, *Fpn*^{ΔCtsk} mature osteoclasts displayed a trend but not a significant increase ($p = 0.07$) in iron content compared with the control cells (Fig. 4B). These inconsistent results may be caused by the

different sensitivity of these two methods. The elevated cellular iron in late stages of osteoclast lineage cells has no effect on the formation of TRAcP⁺ osteoclasts (Fig. 4C), cytoskeleton organization/actin-ring formation, and bone resorption activity (Fig. 4D). These results, along with those shown in Fig. 2, suggest that loss of *Fpn* in mature osteoclasts has little effect on osteoclast differentiation and function *in vivo* and *in vitro*.



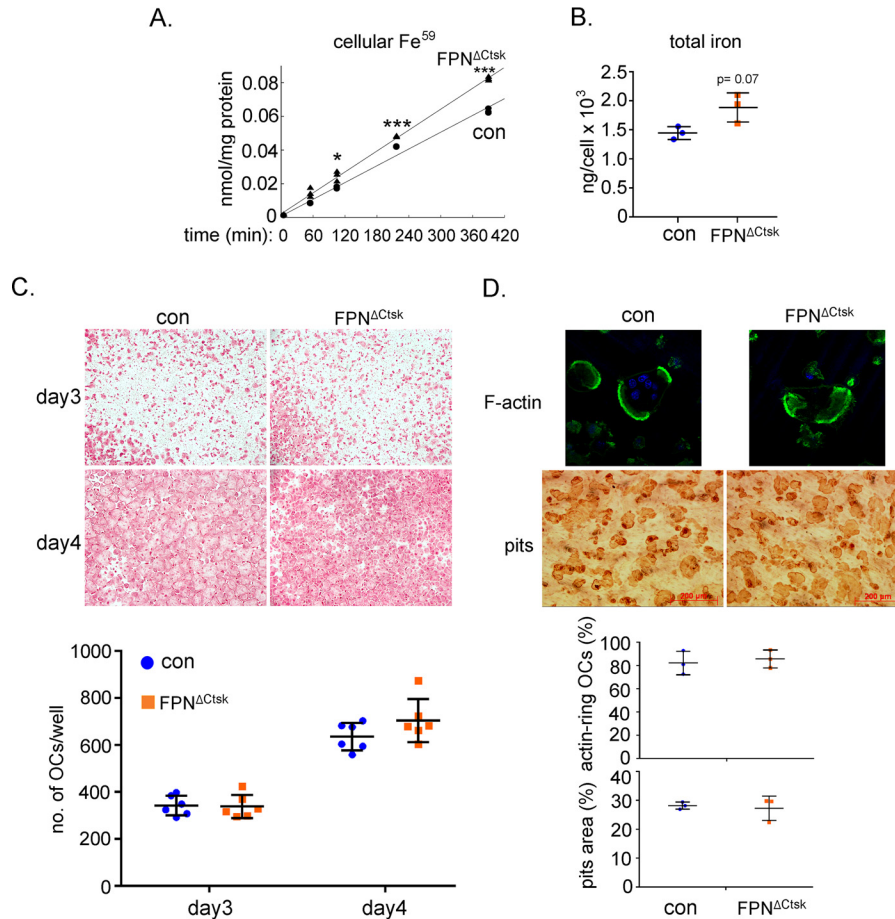


Figure 4. Deletion of *Fpn* in mature osteoclasts has no effects on osteoclast differentiation and function. Bone marrow monocytes were cultured with M-CSF (BMM) or M-CSF + RANKL for 2 and 4 days to generate mononuclear pre-osteoclasts (*pOC*) and mature multinucleated osteoclasts (*OC*), respectively. *A*, intracellular levels of uptaken Tf-Fe⁵⁹ in mature osteoclasts were measured by a gamma counter. The data were normalized by protein concentrations. *n* = 3. *B*, amount of cellular total iron in mature osteoclasts was measured using a colorimetric iron assay method. The data were normalized by osteoclast number in each well of a 6-well plate. *n* = 3. *C*, TRAcP staining of osteoclasts cultured on 48-well plastic tissue culture plates. The number of TRAcP⁺ osteoclasts with more than three nuclei was counted. *n* = 6. *D*, confocal microscopic images (*upper panels*) of filament actin (F-actin, *green*) and nucleus (*blue*) staining in osteoclasts cultured on bone slices. Resorption pits (*lower panels*) were stained with HRP-labeled WGA lectin. The percentage of active osteoclasts (*OCs* with actin rings) to the total number of osteoclasts with more than three nuclei was quantified. The pits area (%) was measured and calculated using ImageJ software (National Institutes of Health). The data shown are representatives from three independent experiments. *, *p* < 0.05; **, *p* < 0.01; ***, *p* < 0.001 versus control (*con*) by one-way ANOVA.

Loss of *Fpn* in monocytes promotes cell proliferation and up-regulates M-CSF-induced AKT activation

Cell proliferation, differentiation, and survival of osteoclast precursor cells are critical cellular processes regulating osteoclastogenesis *in vivo* and *in vitro*. To determine which of these processes are influenced by increased cellular iron, we performed BrdU labeling followed by flow cytometry analysis of control and *Fpn*-deletion BMMs. As shown in Fig. 5*A*, loss of *Fpn* significantly enhanced the population of BrdU⁺ mono-

cytes. Lack of *Fpn* had no impact on survival of osteoclast precursor cells as assayed by Cell-Death ELISA (Fig. 5*B*).

Intracellular signaling pathways activated by M-CSF and RANKL play an essential role in osteoclast differentiation and survival. We next tried to determine whether increased cellular iron induced by *Fpn* deficiency modulates downstream signaling pathways of M-CSF and/or RANKL in BMMs. As presented by Western blottings in Fig. 5*C*, M-CSF induced ERK- and RANKL-stimulated NF- κ B and JNK activations, as monitored

Figure 3. Loss of *Fpn* in BMMs enhances cellular iron accumulation and accelerates osteoclast formation *in vitro*. Bone marrow monocytes were cultured with M-CSF (BMM) or M-CSF + RANKL for 2 and 4 days to generate mononuclear pre-osteoclasts (*pOC*) and mature multinucleated osteoclasts (*OC*), respectively. *A*, mRNA expression of *Fpn*, encoded by *Slc40a1*, was detected by qPCR using a primer specific to the exon 6 of murine *Slc40a1*. *n* = 3. *B*, intracellular levels of uptaken Tf-Fe⁵⁹ in control (*con*) and *Fpn*-deleted (*Fpn*^{ΔLy5M}) BMMs were measured by a gamma counter. The data were normalized by protein concentrations. *n* = 3. *C*, amount of cellular total iron was measured using a colorimetric iron assay kit. The data were normalized by cell number in each well of a 6-well plate. *n* = 3. *D*, TRAcP staining of control and *Fpn*-deleted osteoclastogenic cultures on plastic and bone slices. *E*, quantification of the number of TRAcP⁺ osteoclasts with more than three nuclei per well of a 48-well plate, *n* = 6, and per slice of bovine cortical bone, *n* = 3. *F*, mRNA expression of osteoclast marker genes in osteoclast lineage cells detected by quantitative real-time PCR. *Acp5*, encoding TRAcP; *Nfatc1*, encoding NFATc1; *Ppargc1b*, encoding PGC-1 β . *n* = 3. *G*, protein expression of cathepsin K (*CTSK*), NFATc1, and PGC-1 β during osteoclast differentiation was detected by Western blottings. Tubulin served as loading controls. The densitometry quantification of each band was done by ImageJ (National Institutes of Health). The ratios of band density of CTSK, NFATc1, and PGC-1 β to that of corresponding tubulin are presented. *m*, BMMs; *p*, pre-osteoclasts; *oc*, mature osteoclasts. The representative data from three independent experiments are shown. *, *p* < 0.05; **, *p* < 0.01 versus control (*con*) by one-way ANOVA.

Ferroportin and osteoclast formation

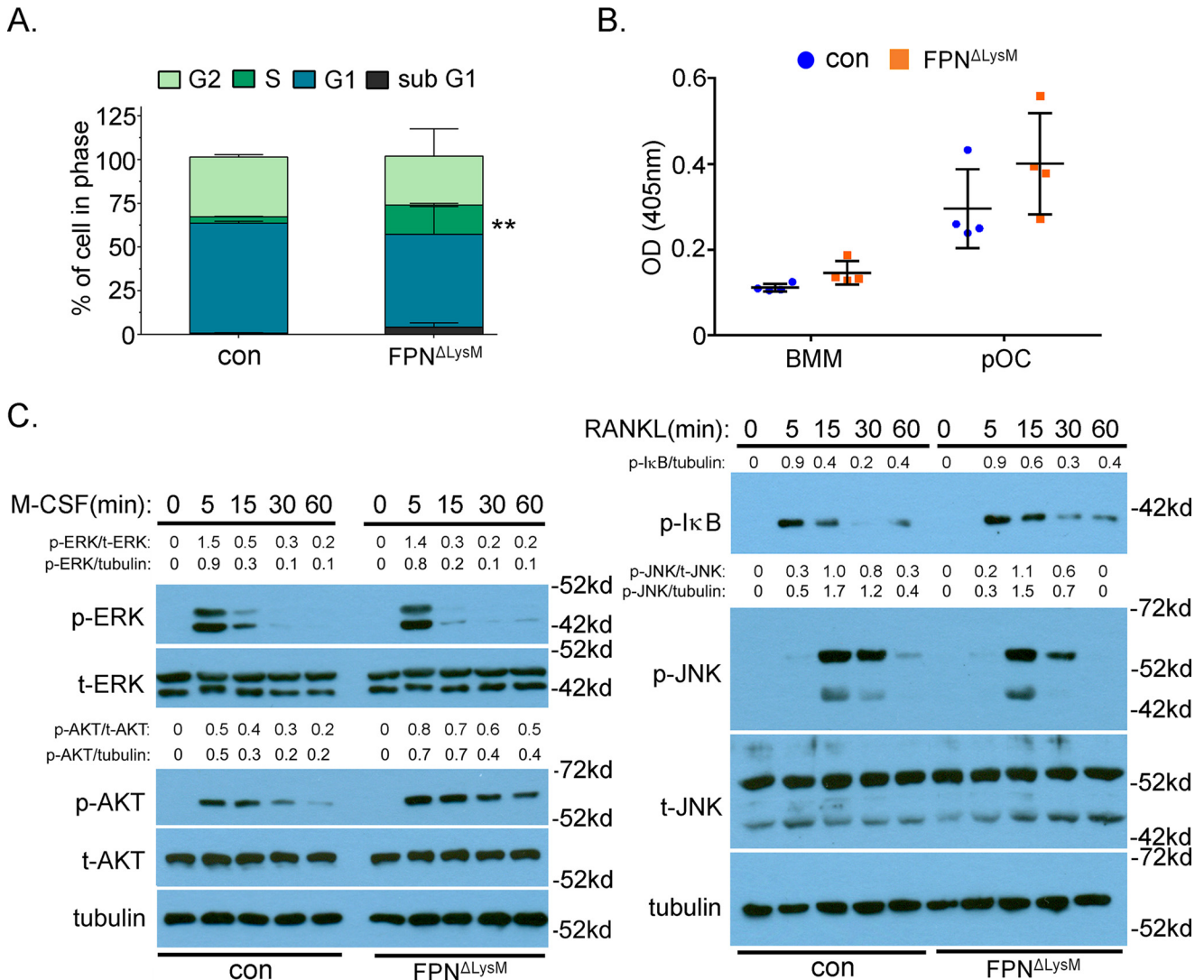


Figure 5. Loss of *Fpn* in BMMs enhances cell proliferation and M-CSF-stimulated AKT activation. BMMs were cultured with M-CSF alone or M-CSF + RANKL for 2 days to generate mononuclear pre-osteoclasts (*pOC*). *A*, cell proliferation and cell cycle progression in BrdU and 7' AAD-labeled control (*con*) and *Fpn*-deleted (*Fpn*^{ΔLysM}) BMMs were analyzed by flow cytometry. *n* = 4. **, *p* < 0.01 versus control by Student's *t* test. *B*, BMMs and *pOC* were serum- and cytokine-starved for 3 h. The apoptosis rate was measured by a cell death detection ELISA. *n* = 4. *C*, Western blotting detection of the signaling pathways downstream of M-CSF and RANKL in BMMs. Total ERK (*t-ERK*), total AKT (*t-AKT*), tubulin, and total JNK (*t-JNK*) served as loading controls. The densitometry quantification of each band was done by ImageJ software (National Institutes of Health). The ratios of band density of phosphorylated ERK (*p-ERK*), AKT (*p-AKT*), IκB (*p-IκB*), and JNK (*p-JNK*) to that of corresponding loading controls are presented. All the data are representative of three independent experiments.

by their phosphorylation status upon stimulation, were indistinguishable between control and *Fpn*-depleted macrophages. Similarly, mRNA expressions of *IκB*, *TNF*, and *IL-6*, canonical downstream target genes of the NF-κB pathway, were the same between control and *Fpn*-depleted osteoclast lineage cells (Fig. S6). Moreover, M-CSF-activated AKT was more prolonged and robust in *Fpn*-null BMMs (Fig. 5C). These findings indicate that increased cellular iron in BMMs stimulates proliferation of osteoclast precursors by up-regulation of the M-CSF-activated AKT pathway that is important for osteoclast precursor cell proliferation (61).

Fpn deletion in osteoclast lineage cells stimulates mitochondrial metabolism but has little effect on mitochondrial mass and ROS production

Mounting evidence indicates that mitochondrial energy metabolism plays a pivotal role in osteoclast differentiation and

function (14, 16). Given that iron is an essential metal for mitochondrial metabolism (34), we next focused on investigating the effects of increased cellular iron on mitochondrial mass and metabolism in osteoclast lineage cells. As shown in Fig. 6A, *Fpn*^{-/-} BMMs displayed a slight decreased mitochondrial mass, as measured by flow cytometry analysis of MitoTracker-stained BMMs. Consistent with this finding, manual quantification of MitoTracker fluorescent intensity in cultured osteoclast lineage cells demonstrated a mild decline of mitochondrial mass in *Fpn*^{-/-} BMMs and pre-osteoclasts compared with control cells. Loss of *Fpn* did not affect mitochondrial membrane potential (Fig. 6, B and C). Accumulation of iron in mature osteoclasts cultured from *Fpn*^{ΔCtsk} mice resulted in a mild increase in mitochondrial mass and elevated mitochondrial membrane potential (right panels of Fig. 6, B and C).

We next measured total and mitochondrion-derived ROS by flow cytometry analysis of dihydroethidium (DHE)- and

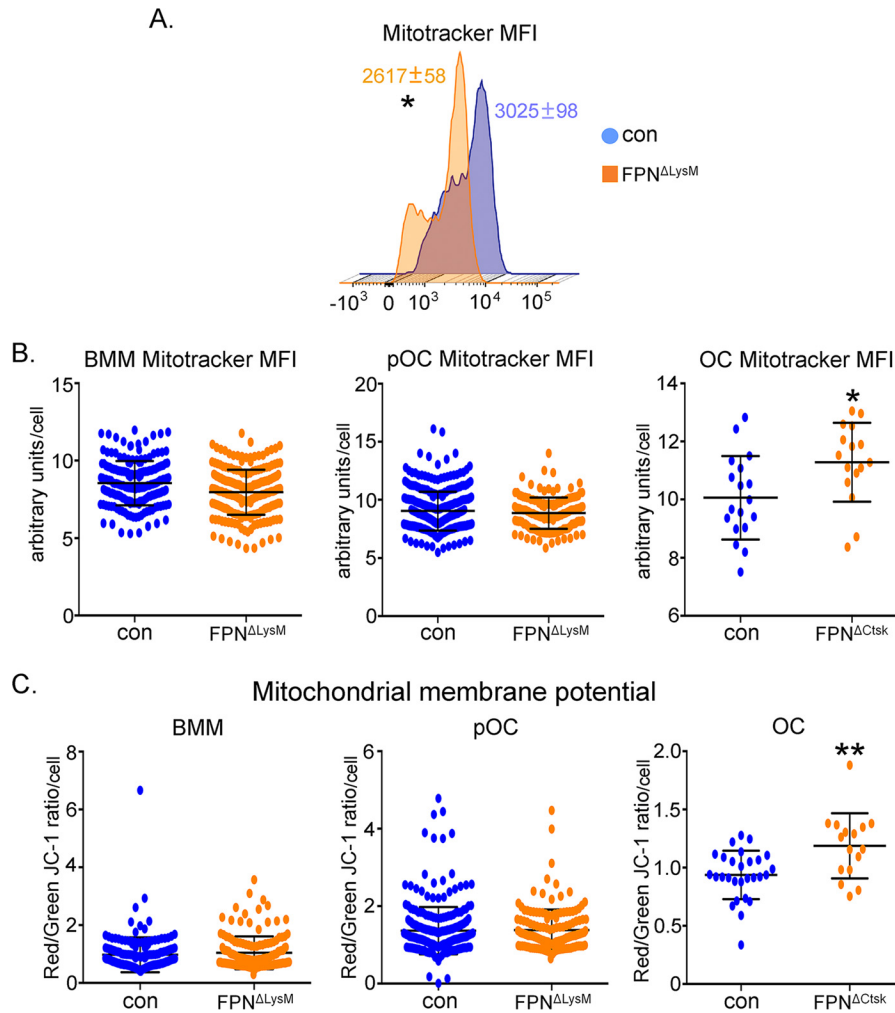


Figure 6. Deletion of *Fpn* in osteoclast lineage cells slightly increases mitochondrial mass and membrane potential only in mature osteoclasts. Bone marrow monocytes were cultured with M-CSF (BMM) or M-CSF + RANKL for 2 and 4 days to generate mononuclear pre-osteoclasts (pOC) and mature multinucleated osteoclasts (OC), respectively. *A*, flow cytometry analysis of mitochondrial mass in MitoTracker Green fluorescence-labeled control (con) and *Fpn*-deleted (*Fpn*^{ΔLysM}) BMMs. *n* = 3. *B*, manual quantification of MitoTracker Green fluorescence index in 100 control and *Fpn*^{ΔLysM} BMMs and pOCs. 25 control and *Fpn*^{ΔCtsk} mature OCs were measured. *C*, mitochondrial membrane potential was measured by dual JC1 staining. Manual quantification was performed in 100 control and *Fpn*^{ΔLysM} BMMs and pOCs and in 25 control and *Fpn*^{ΔCtsk} mature OCs. MitoTracker Green and MitoSOX results were presented as mean fluorescence intensity per cell in arbitrary units.

MitoSOX-stained control and *Fpn*^{ΔLysM} BMMs. As presented in Fig. 7, *A–C*, lack of *Fpn* in BMMs led to a small decrease in the levels of total and mtROS, probably due to the reduced mitochondrial number in these cells. A manual quantification of MitoSOX staining in control and *Fpn*^{−/−} osteoclast lineage cells cultured on glass coverslips confirmed the decreases of mtROS in osteoclast precursor cells but a slight increase of mtROS in mature *Fpn*^{ΔCtsk} osteoclasts (Fig. 7, *D–F*), which also correlates with increased mitochondrial mass in these cells.

To examine the effects of cellular iron on mitochondrial metabolism in osteoclast lineage cells more quantitatively, we measured mitochondrial respiration using the Seahorse Extracellular Flux analyzer in control and *Fpn*^{ΔLysM} BMMs, pre-osteoclasts and mature osteoclasts. As illustrated in Fig. 8*A*, the basal mitochondrial respiration is the direct measure of oxygen consumption rate attributed only to the mitochondrial electron transport chain (ETC). This parameter increased during osteoclast differentiation in both control and *Fpn*^{ΔLysM} pOCs compared with BMMs. Loss of *Fpn* further promoted basal respira-

tion in *Fpn*^{ΔLysM} BMMs and pOCs relative to their control cells (Fig. 8*B*), indicating that iron accumulation enhanced ETC activities in osteoclast precursor cells.

ATP-linked respiration was also measured by exposing cells to oligomycin, an inhibitor of ATP synthase (complex V) (Fig. 8*A*). *Fpn*^{ΔLysM} BMMs and pOCs exhibited higher ATPase-associated activity than control cells, suggesting an increase in ATP demand in these cells (Fig. 8*C*).

Next, maximum respiration was determined by introducing the uncoupler, carbonyl cyanide 4-(trifluoromethoxy)phenylhydrazone (FCCP) to the cells (Fig. 8*A*), which induces maximum OCR that cells can achieve. As shown in Fig. 8*D*, there was a dramatic increase in maximum respiration during osteoclast differentiation in both control and *Fpn*^{ΔLysM} cultures. Increased intracellular iron in *Fpn*^{ΔLysM} pOCs further enhanced this activity relative to control pOCs.

Furthermore, we calculated the cells' reserve respiratory capacity, which is the difference between the maximum and basal respiration that can be utilized in the event of a sudden

Ferroportin and osteoclast formation

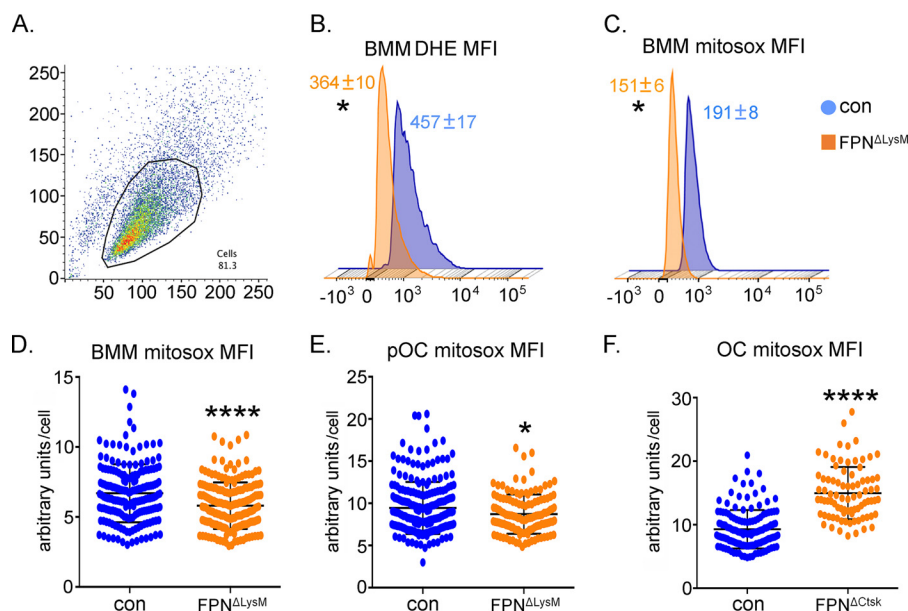


Figure 7. Deletion of *Fpn* in osteoclast precursor cells slightly decreases total and mitochondrion-derived ROS, whereas loss of *Fpn* in mature osteoclasts moderately increases mitochondrial ROS. Bone marrow monocytes were cultured with M-CSF (BMM) or M-CSF + RANKL for 2 and 4 days to generate mononuclear pre-osteoclasts (pOC) and mature multinucleated osteoclasts (OC), respectively. A–C, flow cytometry analysis of total (B) and mitochondrion-derived (C) ROS per cell in control (con) and *Fpn*-deleted (*Fpn*^{ΔLysM}) BMMs. *n* = 3. D–F, manual quantification of MitoSOX Red fluorescence index per cell in 100 control and *Fpn*^{ΔLysM} BMMs and pOCs and in 25 control and *Fpn*^{ΔCtsk} mature OCs. *, *p* < 0.05; ****, *p* < 0.0001 versus con by Student's *t* test. MitoTracker Green and MitoSOX results were presented as MFI per cell in arbitrary units.

energy demand in BMMs and pOCs. We reported this as a percentage for each group in Fig. 8E by using the formula of ((maximum OCR) – (basal OCR))/(maximum OCR)·100. Although both control and *Fpn*^{ΔLysM} pOCs presented higher levels of reserve respiratory capacity than BMMs, *Fpn*^{ΔLysM} BMMs and pOCs displayed significantly less reserve respiratory capacity compared with control cells (Fig. 8E). These data suggest that *Fpn*^{ΔLysM} BMMs and pOCs utilize more reserve respiratory capacity than their control counterparts to meet increased energy demand of accelerated osteoclastogenesis in these cells (see Fig. 3).

When OCR is inhibited using oligomycin, not all basal respiration is halted (Fig. 8A). The residual OCR is the measure of the protons pumped through ETC, which consumes oxygen without generating any ATP (due to inhibited ATP synthase activity by the drug), and referred to the proton leak measurements presented in Fig. 8F. There was an increase in proton leak in *Fpn*^{ΔLysM} pOCs, which in turn resulted in the decreased coupling efficiency (ratio of ATP-linked OCR to basal OCR) in these cells (Fig. 8G).

Finally, we examined the nonmitochondrial respiration, which was the remaining OCR when the ETC activity was completely abolished by a mixture of rotenone/antimycin A. This parameter reflects the portion of cellular respiration by oxygen-consuming enzymes such as NADPH oxidases, heme oxygenases, and/or lipoxygenases. As demonstrated in Fig. 8H, nonmitochondrial OCR was increased during osteoclast differentiation in both control and *Fpn*^{ΔLysM} cultures, and this increase was more pronounced in the absence of *Fpn* in BMMs and pOCs. Given that some of these cytosolic enzymes contain heme, the increased cellular iron in *Fpn*-null cells could also promote the activities of these enzymes, thereby resulting in increased oxygen consumption that is not associated with

mitochondrial ETC activity. Because NADPH oxidases, heme oxygenases, and lipoxygenases have been reported to regulate osteoclasts (28, 29, 62, 63), it will be very interesting to further investigate how intracellular iron regulates the activities and ROS production of these enzymes in the future.

To assess the influences of increased cellular iron on bioenergetics and mitochondrial respirations in mature OCs, we used cells isolated and cultured from the control and *Fpn*^{ΔCtsk} mice. These cells showed the same differentiation capacity toward to OCs (Fig. 4). Although there were robust rises (40–100-fold) in mitochondrial basal, ATP-linked, and maximum respiration in mature OCs compared with BMMs and pOCs, the differences of all parameters of the Seahorse assay between the control and *Fpn*^{ΔCtsk} mature OCs were very minor (Fig. 9).

Discussion

Osteoporosis, osteopenia, and pathological bone fractures are frequent complications of iron-overload conditions either occurring in hereditary hemochromatosis or caused by multiple blood transfusions in the treatment of thalassemia and sickle cell disease (46, 47, 64, 65). In congenital dyserythropoietic anemia and sideroblastic anemia, increased erythroid destruction often leads to nontransfusional iron overload (66). Recent studies in genetic mouse models of iron overload diseases (67–69) and in acquired iron-excess murine models (54, 55, 70) have indicated that increased bone resorption and/or decreased bone formation are culprits of bone loss induced by excess iron.

To elucidate the direct role of cellular iron homeostasis in osteoclast lineage cells, we generated *Fpn* myeloid precursor (*Fpn*^{ΔLysM}) and mature osteoclast (*Fpn*^{ΔCtsk}) deletion mice. Consistent with the previous report by Zhang *et al.* (43), *Fpn* deficiency resulted in a mild increase of iron accumulation in

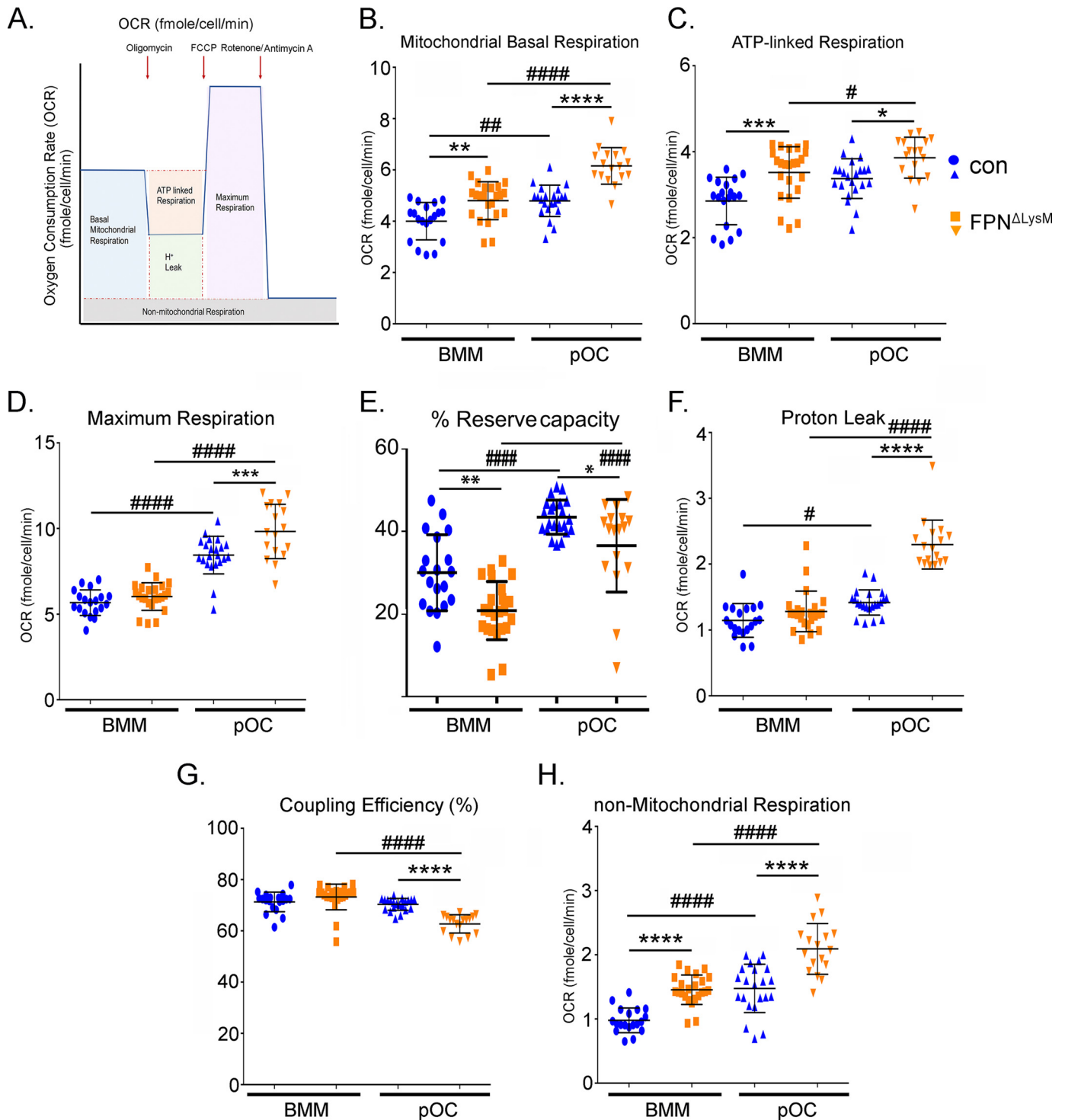


Figure 8. Loss of *Fpn* in osteoclast precursor cells increases overall mitochondrial and nonmitochondrial respirations. BMMs were cultured with M-CSF alone or M-CSF + RANKL for 2 days to generate mononuclear pre-osteoclasts (pOC). *A*, cartoon illustration of oxygen consumption analyzed by a Seahorse Extracellular Flux analyzer. *B–H*, different fractions of mitochondrial and nonmitochondrial respirations per cell in control (*con*) and *Fpn*-deleted (*Fpn*^{ΔLysM}) BMMs and pOCs were measured by Seahorse. *n* = 18–24. *, *p* < 0.05; **, *p* < 0.01; ***, *p* < 0.001; ****, *p* < 0.0001 versus corresponding control; #, *p* < 0.05; ##, *p* < 0.01; ####, *p* < 0.0001 versus corresponding BMM by one-way ANOVA.

bone marrow macrophages and osteoclasts. Whereas elevated intracellular iron level in osteoclast precursor cells accelerated osteoclastogenesis *in vitro* and *in vivo*, the slightly increased cellular iron by *Fpn* deletion in mature osteoclasts had little effect on osteoclast formation and function in cultures and did not influence bone modeling and remodeling in mice.

Interestingly, the decline in trabecular bone mass and cortical bone thinning observed in *Fpn*^{ΔLysM} mice was more pronounced in female mice. The exact explanation(s) and mechanism(s) underlying this gender-specific difference of iron overload on bone metabolism are unknown. Although iron overload and hypogonadism are both common complications

Ferroportin and osteoclast formation

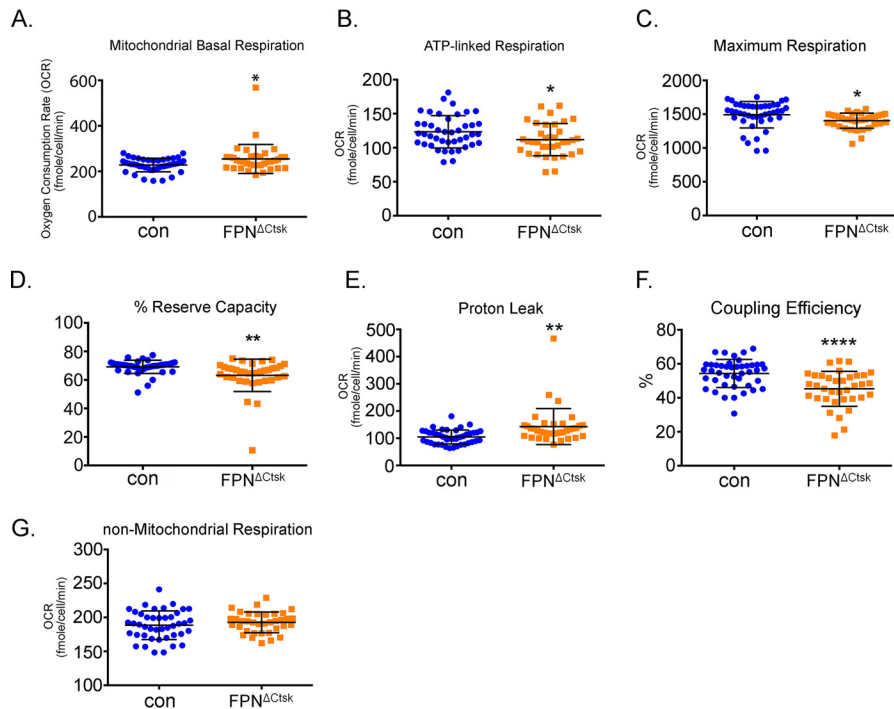


Figure 9. Deletion of *Fpn* in mature osteoclasts exhibits different effects on mitochondrial and nonmitochondrial respirations compared with osteoclast precursor cells. Bone marrow monocytes isolated from long bones of control (*con*) and *Fpn*-deleted (*Fpn*^{ΔCtsk}) mice were cultured with M-CSF + RANKL for 4 days to generate mature multinucleated osteoclasts (OC). Different fractions of mitochondrial and nonmitochondrial respirations per osteoclast were measured by Seahorse. *n* = 36–43. *, *p* < 0.05; **, *p* < 0.01; ****, *p* < 0.0001 versus control.

in iron overload diseases (71), there is no direct evidence whether FPN or systemic iron content affects estrogen and androgen levels. Conversely, both sex hormones have been shown to regulate iron homeostasis through FPN and its upstream modulator hepcidin, which binds to FPN and induces FPN internalization and degradation (72–74). It is clear that estrogen regulates FPN and hepcidin expression via an estrogen-response element in the promoter region of these two genes (73, 75). How androgen directly modulates iron status under physiological condition remains unknown.

A 2–3-fold increase in serum ferritin level has been reported in postmenopausal women (76, 77). Two recent clinical cross-sectional studies reveal a significant correlation between iron overload and low bone mass/fragility fractures in postmenopausal women (78, 79). A recent large-scale retrospective longitudinal study demonstrates that bone loss rate in postmenopausal women is much faster than age-matched men despite the fact that the serum ferritin level in men is higher than in women (80). This finding is consistent with our findings in *Fpn*^{ΔLysM} mice. Sex-dependent changes in bone mineral density and bone resorption have been recently reported in a thalassemic knockin mouse model (69).

Administration of hepcidin in osteoclastogenic cultures of BMMs has been shown to reduce the protein level of FPN which, in turn, leads to increased cellular iron in BMMs and promotes osteoclast formation (81). These findings are in accordance with ours obtained in *Fpn*^{−/−} *in vitro* experiments. Therefore, it is possible that estrogen inhibits osteoclastogenesis by maintaining the FPN level and reducing intracellular iron concentration in osteoclast precursor cells. This previ-

ously unknown function of estrogen on osteoclasts needs further investigation in the future.

Increasing extracellular iron by adding Tf or different forms of iron, such as FeSO₄, FeCl₃, and iron ammonium citrate into the cultures of BMMs, promotes M-CSF- and RANKL-induced osteoclastogenesis *in vitro* (14, 70, 82). This stimulatory effect of excess iron on osteoclast precursor cells is, at least in part, due to enhanced activation of the NF-κB pathway by RANKL and ROS production. Treatment of osteoclastogenic cultures with the iron chelator desferrioxamine or anti-oxidant *N*-acetylcysteine abolishes iron-provoked osteoclast formation and NF-κB activation (14, 70). Thus, stimulation of NF-κB pathway plays an important role in excess iron-induced osteoclastogenesis.

In this study, we have shown that a higher level of intracellular iron induced by *Fpn* deletion in osteoclast precursors enhances osteoclast formation and osteoclast-specific gene expression. At the molecular level, however, *Fpn* deletion amplifies M-CSF-stimulated PI3K/AKT activation and macrophage proliferation but has minimal influence on the RANKL-activated NF-κB pathway and the expression of its target genes, such as *IκB*, *Tnf*, and *Il-6*. This discrepancy between our finding and the previous reports in terms of NF-κB activation by iron is likely due to the reason that *Fpn* depletion only induces a mild increase in intracellular iron as compared with the high concentration of iron used in most previous studies.

Iron is a crucial element for mitochondrial metabolism. Iron-containing heme and Fe-S clusters are integral co-factors of mitochondrial respiratory complex I to IV that are important for the stability and functions of these complexes (34). Therefore, an increase in the cellular iron caused by *Fpn* depletion

directly promotes mitochondrial complex I to IV activities and augments both basal and maximum mitochondrial respiration in osteoclast lineage cells. The enhanced activity and electron transfer of complex I to IV generate more proton gradient across the mitochondrial membrane that, in turn, facilitates the ATP-linked respiration by complex V, although it does not contain heme and Fe-S clusters. In addition to the complexes I to IV, heme and Fe-S clusters are also key co-factors of the critical cytoplasmic enzymes involving energy metabolism, DNA and RNA dynamics, and DNA damage response. Thus, *Fpn*^{-/-} osteoclast precursors exhibit a significant increase in nonmitochondrial respiration. Because iron and iron-containing proteins are involved in a variety of mitochondrial and nonmitochondrial pathways, how iron homeostasis regulates cellular metabolism in osteoclast lineage cells warrants the detailed mechanistic studies using the state-of-the-art approaches by genomics, proteomics, and metabolomics in the future.

Mitochondrial respiration also produces ROS, which are harmful at high levels, although they can modulate signal transduction at low concentrations. Moreover, mtROS play an important role in regulation of osteoclasts (30–34). Although the mild accumulation of iron in *Fpn*-deficient BMMs leads to an overall increase in mitochondrial respiration, the total and mtROS levels remain little changed in these cells. It is likely that sufficient iron in the mitochondria of *Fpn*^{-/-} BMMs might optimize the activities of the electron transportation chain protein complexes to produce more ATP while avoiding generation of unwanted ROS. Alternatively, increased activities of ROS removal pathways in *Fpn*-deficient cells maintain the redox balance in the situation of excess iron.

In summary, we have shown here that deletion of FPN caused a mild increase in cellular iron level in osteoclast precursor and mature cells. However, loss of *Fpn* in precursor but not mature osteoclasts led to increased osteoclastogenesis and decreased bone mass in female mice. *In vitro* mechanistic studies revealed that elevated intracellular iron promoted macrophage proliferation and enhanced expression of NFATc1 and PGC-1 β , two transcription factors critical for osteoclast differentiation. The moderate iron excess induced by *Fpn* deletion had no effects on osteoclast survival. Although the increased iron stimulated global mitochondria metabolism in osteoclast lineage cells, it had little influence on mitochondrial mass and ROS production.

Experimental procedures

Mice

Slc40a1-floxed mice (129S-*Slc40a1*^{tm2Nca/J}, stock number 017790) in congenic 129 background were obtained from The Jackson Laboratory. *LysM*-Cre mice (stock number 004781) in C57BL6/129 mixed background were originally purchased from The Jackson Laboratory and were backcrossed to congenic C57BL6J background in our laboratory (83). *Ctsk*-Cre mice in C57BL6J background were kindly provided by Dr. Nakamura (Keio University, Tokyo, Japan) (58). The littermates of control (+/+; *LysM*-Cre and +/+; *Ctsk*-Cre) and conditional knockout (*Fpn*-flox/flox; *LysM*-Cre and *Fpn*-flox/flox; *Ctsk*-Cre) mice in a mixed background were used for *in vivo*

analysis of skeletal phenotypes. The sequences of genotyping primers and PCR protocols for genotyping these mice followed those provided by The Jackson Laboratory. We genotyped offspring of *Ctsk*-Cre mice by PCR using the following primers: P1N (5'-CCTAATTATTCCTTCGCCAGGATG-3'), P2N (5'-CCAGGTTATGGGCAGAGATTTGCTT-3'), and P3N (5'-CACCGGCATCAACGTTTTCTTTTCG-3'). All animal protocols and procedures used in this study were approved by the Institutional Animal Care and Use Committees of the University of Arkansas for Medical Sciences.

Micro-CT

The left femurs and L4 vertebrae of 2-month-old control and *Fpn* conditional knockout mice were cleaned of soft tissues and fixed in 10% Millonig's formalin with 0.5% sucrose for 24 h. The bone samples were serially dehydrated into 100% ethanol. The bones were loaded into a 12.3-mm diameter scanning tube and were imaged in a μ CT (model μ CT40, Scanco Medical). We integrated the scans into 3D voxel images (1024 \times 1024 pixel matrices for each individual planar stack) and used a Gaussian filter ($\sigma = 0.8$, support = 1) to reduce signal noise. A threshold of 200 was applied to all scans, at medium resolution ($E = 55$ kilovolt peak, $I = 145 \mu\text{A}$, integration time = 200 ms).

Histology and bone histomorphometry

The right femurs of 2-month-old control and *Fpn* conditional knockout mice were fixed in 10% Millonig's formalin for 24 h and were decalcified in 14% EDTA for 7–10 days. The bones were embedded in paraffin before obtaining 5- μm longitudinal sections. After removal of paraffin and rehydration, sections were stained for TRAcP and counter-stained with methyl green. The histomorphometric measurements of trabecular bone and osteoclast and osteoblast surface were done with a digitizer tablet (OsteoMetrics, Inc., Decatur, GA) interfaced to a Zeiss Axioscope (Carl Zeiss, Thornwood, NY) with a drawing tube attachment.

Serum TRAcP-5b, PINP, CTx-I, and ferritin ELISA

Blood samples from each mouse were collected retro-orbitally under inhalation of a 2% isoflurane/oxygen mix anesthesia immediately prior to sacrifice. Serum was obtained by centrifugation of blood in a serum separator tube (catalogue no. 02-675-188, Thermo Fisher Scientific). The serum levels of TRAcP-5b, PINP, CTx-I, and ferritin were measured by a mouse TRAP (TRAcP 5b) kit (SB-TR103, Immunodiagnostic Systems), rat/mouse PINP EIA kit (AC-33F1, Immunodiagnostic Systems), RatLaps (CTx-I), EIA (AC-06F1, Immunodiagnostic Systems), and mouse ferritin ELISA kit (LS-F20757, LifeSpan BioSciences, Inc) following their instructions.

Antibodies and reagents

The antibodies used in this study were obtained from the following resources: mouse monoclonal anti-cathepsin K (clone 182-12G5, MilliporeSigma); mouse monoclonal anti-NFATc1 (catalogue no. sc-7294, Santa Cruz Biotechnology); rabbit polyclonal anti-PGC-1 β antibody (catalogue no. ab130741, Abcam); mouse monoclonal anti- α -tubulin (clone DM1A, MilliporeSigma), and the following antibodies from

Ferroportin and osteoclast formation

Cell Signaling Technology: rabbit monoclonal anti-phospho-Akt (catalogue no. 4058); mouse monoclonal anti-Akt (catalogue no. 2920); mouse monoclonal anti-phospho-ERK1/2 (catalogue no. 9106); rabbit polyclonal anti-ERK1/2 (catalogue no. 9102); mouse monoclonal anti-phospho-IKB- α (catalogue no. 9246); rabbit polyclonal anti-IKB- α (catalogue no. 9242); mouse monoclonal anti-phospho-JNK (catalogue no. 9255); and rabbit polyclonal anti-JNK (catalogue no. 9252).

Cell culture α -MEM (catalogue no. 78-5077EB) and $10 \times$ trypsin/EDTA (catalogue no. 15400-054) were purchased from Life Technologies, Inc. $10 \times$ penicillin/streptomycin/L-glutamine (PSG) (catalogue no. G1146) was obtained from Sigma. Fetal bovine serum was purchased from Hyclone.

BMM and osteoclast cultures

BMMs were prepared as described previously (84). Briefly, whole bone marrow was extracted from the tibia of 2-month-old control and *Fpn* conditional knockout mice. Red blood cells were lysed in buffer (150 mM NH_4Cl , 10 mM KNCO_3 , 0.1 mM EDTA, pH 7.4) for 5 min at room temperature. Bone marrow cells (5×10^6) were plated onto a 100-mm Petri dish and cultured in α -10 medium (α -MEM, 10% heat-inactivated fetal bovine serum, $1 \times$ penicillin/streptomycin/L-glutamine solution) containing 1/10th volume of CMG 14-12 (conditioned medium supernatant containing recombinant M-CSF at $1 \mu\text{g/ml}$ (85)) for 4–5 days. Fresh media and CMG 14-12 supernatant were replaced every other day. BMMs were then cultured with 1/100th volume of CMG 14-12 culture supernatant alone for monocytes or cultured with 1/100th volume of CMG 14-12 culture supernatant plus 100 ng/ml recombinant RANKL for 2 and 4 days to generate pre-osteoclasts and mature osteoclasts, respectively.

TRAcP staining and resorption pit staining

Osteoclasts cultured on plastic or cortical bovine bone slices were fixed with 4% paraformaldehyde/PBS for 20 min at room temperature, and TRAP was stained with NaK tartrate and naphthol AS-BI phosphoric acid (MilliporeSigma) as described previously (86). Photomicrographs were taken with a stereomicroscope with a digital camera (Discovery V12 and AxioCam; Carl Zeiss, Inc.). The number of osteoclasts with more than three nuclei was counted and analyzed in a double-blinded manner.

Mature osteoclasts grown on bone slices were removed with a soft brush, and resorption pits were stained as described previously (87). In brief, bone slices were incubated with $20 \mu\text{g/ml}$ peroxidase-conjugated wheat germ agglutinin (WGA) lectin (catalogue no. L-7017, MilliporeSigma) for 30–60 min at room temperature. After washing in PBS twice, bone chips were incubated with 0.52 mg/ml 3,3'-diaminobenzidine (D-5905, Sigma) and 0.03% H_2O_2 for 30 min. Samples were mounted with 80% glycerol/PBS and photographed with Zeiss AxioPlan2 microscope equipped with a Olympus DP73 digital camera. The resorbed area/bone slice was quantified by ImageJ software (National Institutes of Health), and the percentage of pit area *versus* that of the whole bone slice was calculated.

Fluorescent staining of actin filament and nuclei

Osteoclasts cultured on bovine cortical bone slices were fixed with 4% paraformaldehyde/PBS for 20 min at room temperature. The staining of filamental actin and nuclei was then performed following the protocol described previously (88). The percentage of active osteoclasts (actin-ring bearing osteoclasts) in total osteoclasts per bone slice was counted under the microscope and calculated.

RNA isolation and qPCR

Total RNA was purified using an RNeasy mini kit (catalogue no. 74104, Qiagen) according to the protocol of the manufacturer. First-strand cDNAs were synthesized from 0.5–1 μg of total RNA using the high-capacity cDNA reverse transcription kit (catalogue no. 4368813, Applied Biosystems/Thermo Fisher Scientific) following the instructions of the manufacturer. TaqMan quantitative real-time PCR was performed using the following primers from Applied Biosystems: *Acp5* (Mm00475698_m1); *NFATc1* (Mm00479445_m1); *Ppargc1b* (Mm00504720_m1); and *Mrps2* (Mm03991065_g1). The custom-designed TaqMan assay primer of the exon 6 of murine *Slc40a1* was purchased from Thermo Fisher Scientific. Samples were amplified using the StepOnePlus real-time PCR system (Life Technologies, Inc.) with an initial denaturation at 95°C for 10 min, followed by 40 cycles of 95°C for 15 s and 60°C for 1 min. The relative cDNA amount was calculated by normalizing to that of the mitochondrial gene *Mrps2*, which is steadily expressed in both BMMs and osteoclasts, using the ΔCt method.

DNA isolation and gene copy number determination

Soft tissues, tibiae, and vertebrae were collected from three mice/genotype. The osteocyte enriched cortical bone was prepared as follows. The proximal and distal ends of the tibia were cut off, and the bone marrow was flushed out completely. The periosteum was scraped away from bone surface. The remaining cortical bones were incubated in 14% EDTA for 1 week. The genomic DNAs of the cells and tissues were purified using DNeasy Blood and Tissue kit (Qiagen) according to the manufacturer's protocol. The custom-designed TaqMan assay primer of exon 6 of murine *Slc40a1* was purchased from Thermo Fisher Scientific. The gene copy number was normalized to murine transferrin receptor 1 locus (Thermo Fisher Scientific).

Western blotting

Cultured cells were washed with ice-cold PBS twice and lysed in $1 \times$ RIPA buffer (catalogue no. R-0278, MilliporeSigma) containing 1 mM DTT and Complete Mini EDTA-free protease inhibitor mixture (catalogue no. 04693159001, MilliporeSigma). After incubation on ice for 30 min, the cell lysates were clarified by centrifugation at 14,000 rpm for 15 min at 4°C . The protein concentration of each sample was quantified using a detergent-compatible protein assay kit (catalogue no. 5000111, Bio-Rad). The equal amounts of total protein for each lane were loaded to 8 or 10% SDS polyacrylamide gels and transferred electrophoretically onto polyvinylidene difluoride

membrane (catalogue no. IPVH00010, MilliporeSigma) by a semi-dry blotting system (Bio-Rad). The membrane was blocked in 5% fat-free milk or 5% BSA in TBS for 1 h and incubated with primary antibodies at 4 °C overnight followed by secondary antibodies conjugated with horseradish peroxidase (Santa Cruz Biotechnology). After rinsing three times with TBS containing 0.1% Tween 20, the membrane was subjected to Western blot analysis with enhanced chemiluminescent detection reagents (catalogue no. WBKLS0100, MilliporeSigma). The densitometry quantification of protein bands was performed using ImageJ software (National Institutes of Health).

Immunofluorescence and confocal laser-scanning microscopy

Osteoclasts cultured on bone slices were fixed with 4% paraformaldehyde in PBS for 20 min. Cells were then permeabilized with 0.1% Triton X-100/PBS for 10 min. Filament actin was labeled with Alexa-488 Fluor phalloidin (catalogue no. A12379, Invitrogen/Thermo Fisher Scientific), and the nucleus was stained with DAPI for 30 min as we did in our previous publication (89). Samples were mounted with 80% glycerol/PBS. Immunofluorescence-labeled cells were observed using a Carl Zeiss fluorescence microscope equipped with a CCD camera and analyzed using a Zeiss spectral confocal laser-scanning microscope equipped with Airyscan (LSM880, Zeiss Microsystems).

Transferrin Fe⁵⁹ uptake assay and colorimetric total iron measurement

Mouse apo-transferrin (Sigma) was labeled with ⁵⁹Fe by a slight modification of the method of Garrick *et al.* (90). Instead of using dialysis to separate unbound ⁵⁹Fe, the labeled Tf was gel-filtered on a Sephadex G-50 column. For Tf-dependent ⁵⁹Fe influx measurements, 25 μg of ⁵⁹Fe-labeled Tf was added to each well of a 6-well plate with 3 ml of medium and incubated in a CO₂ incubator (37 °C, 5% CO₂) with rotation at 80 rpm. At various times after adding labeled Tf, the medium was aspirated, and cells were washed gently three times with 2 ml of cold PBS. Wells were extracted with 1 ml of 0.1 N NaOH; radioactivity was determined on a 0.5-ml aliquot, and protein (Bio-Rad) was determined on 25 μl of the extract.

To measure cellular iron, cells cultured in 6-well plates were collected in 50 μl of the Iron Assay Buffer provided in an Iron Assay kit (ab83366, Abcam) and were homogenized with pellet pestles associated with a motor (Z359947, MilliporeSigma). The cells lysates were centrifuged at 15,000 rpm for 10 min. The supernatants proceeded to measure the total iron (Fe²⁺ and Fe³⁺) concentration following the manufacturer's protocol.

BrdU labeling and flow cytometry

For cell proliferation and cell-cycle analysis, BMMs were lifted by 1 × trypsin/EDTA and were resuspended in cold PBS at 1 × 10⁶/ml. The cells were fixed with 70% ethanol and then were labeled with 10 μmol/liter BrdU for 2 h. BrdU incorporation was detected using Alexa Fluor 488-conjugated mouse anti-BrdU antibody (BD Biosciences-Pharmingen) followed by 25 μg/ml 7-aminoactinomycin-D (7-AAD) staining (BD Biosciences-Pharmingen). The cell cycle analysis was performed by flow cytometry.

Total and mtROS measurements

Steady-state levels of ROS were measured using the fluorescent dyes, DHE (for total ROS) and MitoSOX red (for mtROS) purchased from Invitrogen. BMMs were trypsinized and washed with 5 mM/liter pyruvate containing PBS once and then labeled with DHE (5 μM, in 0.1% DMSO, 40 min) or MitoSOX (2 μM, in 0.1% DMSO, 15 min) at 37 °C. After labeling, cells were kept on ice. Samples were analyzed using an LSRFortessa flow cytometer (BD Biosciences Immunocytometry Systems, Inc.) (excitation 405 nm, emission 585/25-nm bandpass filter). The mean fluorescence intensity (MFI) of 10,000 cells was analyzed in each sample and corrected for autofluorescence from unlabeled cells. mtROS were also visualized using epifluorescence. Cells were plated on glass bottom dishes, cultured, and differentiated as described. BMMs, pre-osteoclasts, and mature osteoclasts were washed with PBS, and monolayers were then labeled with MitoSOX Red (2 μM in 0.1% DMSO), for 15 min in 5 mM/liter pyruvate containing Dulbecco's PBS at 37 °C. Images were acquired using EVOS fluorescence microscope and analyzed using ImageJ software.

Mitochondrial mass and membrane potential measurements

Mitochondrial content and mitochondrial membrane potential were measured using MitoTracker Green fluorescence and JC1 labeling, respectively, using flow cytometry (BMMs) and fluorescence microscopy (BMMs, preosteoclasts, and osteoclasts). Briefly, the BMMs were washed with PBS and incubated with MitoTracker Green (50 nM) (Invitrogen) for 15 min at 37 °C. The probe was then washed off, and cells were resuspended in PBS, filtered through a mesh, and analyzed using a BD LSRFortessa flow cytometer (BD Biosciences Immunocytometry Systems). Ten thousand cells were gated on FSC and SSC to approximate live cells. These cells were then analyzed for fluorescence in the FL1 channel (excitation 488 nm and emission 530/30-nm bandpass filter). For estimation of mitochondrial membrane potential, the BMMs were labeled in serum-free medium containing 5 μg/ml JC-1 (Invitrogen). Samples were incubated at 37 °C for 15 min. Cells were washed to remove unbound JC-1 and collected, filtered, and analyzed via flow cytometry. Ten thousand cells were gated on forward scatter (FSC) and side scatter (SSC) to approximate live cells. These cells were then analyzed for fluorescence in the FL1 channel (excitation 488 nm and emission 530/30-nm bandpass filter) and in the FL2 channel (excitation 488 nm and emission 585/42-nm bandpass filter). The ratio of FL2/FL1 was plotted as a measure of mitochondrial membrane potential. These experiments were repeated with the BMMs, pre-osteoclasts, and mature osteoclasts that were cultured on glass bottom dishes, using EVOS fluorescence microscope, and the images were analyzed using ImageJ software.

Seahorse mitochondrial flux analysis

The BMMs were plated in Seahorse XF96 cell culture plates. The cells received 100 ng/ml recombinant RANKL for differentiation at day 2 (for pre-osteoclasts) or day 4 (for mature osteoclasts). On the day of respiratory function measurements, the media in the wells were changed to unbuffered Dulbecco's modified Eagle's medium supplemented with 4 mM glutamate

Ferroportin and osteoclast formation

and incubated in a non-CO₂ incubator for 1 h at 37 °C. Three baseline measurements were acquired before injection of mitochondrial inhibitors or uncouplers. OCR measurements were taken after sequential addition of oligomycin (10 μM), FCCP (5 μM), and rotenone/antimycin A mixture (10 μM). Oxygen consumption rates were calculated by the Seahorse XF-96 software and represent an average of three measurements on 18–24 different wells. The rate of measured oxygen consumption was reported as fmol of O₂ consumed per min per cell.

Statistics

For all graphs, data are represented as the mean ± S.D. For comparison of two groups, data were analyzed using a two-tailed Student's *t* test. For comparison of more than two groups, data were analyzed using one-way ANOVA, and the Bonferroni procedure was used for Tukey comparison. A *p* value of less than 0.05 was considered significant.

Author contributions—L. W., B. F., T. F., K. K., A. G., C. L., J. Q. F., M. L. J., J. Z., N. A.-B., and H. Z. data curation; L. W., B. F., T. F., K. K., A. G., C. L., J. Q. F., M. L. J., J. Z., and N. A.-B. formal analysis; L. W., B. F., T. F., K. K., A. G., C. L., J. Q. F., M. L. J., J. Z., and N. A.-B. investigation; L. W., B. F., T. F., K. K., A. G., C. L., J. Q. F., M. L. J., J. Z., and N. A.-B. methodology; L. W., B. F., T. F., J. Z., N. A.-B., and H. Z. writing—original draft; J. Z., N. A.-B., and H. Z. supervision; J. Z., N. A.-B., and H. Z. funding acquisition; J. Z., N. A.-B., and H. Z. validation; J. Z., N. A.-B., and H. Z. project administration; H. Z. conceptualization.

Acknowledgments—The Digital Microscopy and Flow Cytometry Cores at the University of Arkansas for Medical Sciences are acknowledged for technical support. We thank Erin Hogan for help with microscopy.

References

- Boyle, W. J., Simonet, W. S., and Lacey, D. L. (2003) Osteoclast differentiation and activation. *Nature* **423**, 337–342 [CrossRef Medline](#)
- Harada, S., and Rodan, G. A. (2003) Control of osteoblast function and regulation of bone mass. *Nature* **423**, 349–355 [CrossRef Medline](#)
- Crockett, J. C., Rogers, M. J., Coxon, F. P., Hocking, L. J., and Helfrich, M. H. (2011) Bone remodelling at a glance. *J. Cell Sci.* **124**, 991–998 [CrossRef Medline](#)
- Zaidi, M. (2007) Skeletal remodeling in health and disease. *Nat. Med.* **13**, 791–801 [CrossRef Medline](#)
- Novack, D. V., and Teitelbaum, S. L. (2008) The osteoclast: friend or foe? *Annu. Rev. Pathol.* **3**, 457–484 [CrossRef Medline](#)
- Ross, F. P., and Teitelbaum, S. L. (2005) $\alpha\text{v}\beta 3$ and macrophage colony-stimulating factor: partners in osteoclast biology. *Immunol. Rev.* **208**, 88–105 [CrossRef Medline](#)
- Takeshita, S., Faccio, R., Chappel, J., Zheng, L., Feng, X., Weber, J. D., Teitelbaum, S. L., and Ross, F. P. (2007) c-Fms tyrosine 559 is a major mediator of M-CSF-induced proliferation of primary macrophages. *J. Biol. Chem.* **282**, 18980–18990 [CrossRef Medline](#)
- Boyce, B. F. (2013) Advances in the regulation of osteoclasts and osteoclast functions. *J. Dent. Res.* **92**, 860–867 [CrossRef Medline](#)
- Nakashima, T., Hayashi, M., and Takayanagi, H. (2012) New insights into osteoclastogenic signaling mechanisms. *Trends Endocrinol. Metab.* **23**, 582–590 [CrossRef Medline](#)
- Takayanagi, H., Kim, S., Koga, T., Nishina, H., Isshiki, M., Yoshida, H., Saiura, A., Isobe, M., Yokochi, T., Inoue, J., Wagner, E. F., Mak, T. W., Kodama, T., and Taniguchi, T. (2002) Induction and activation of the transcription factor NFATc1 (NFAT2) integrate RANKL signaling in ter-

- minal differentiation of osteoclasts. *Dev. Cell* **3**, 889–901 [CrossRef Medline](#)
- Chang, H. (1931) Mitochondria in osteoclasts. *Anat. Rec.* **49**, 30–35
- Holtrop, M. E., and King, G. J. (1977) The ultrastructure of the osteoclast and its functional implications. *Clin. Orthop. Relat. Res.* 1977, 177–196 [Medline](#)
- Scott, B. L., and Pease, D. C. (1956) Electron microscopy of the epiphyseal apparatus. *Anat. Rec.* **126**, 465–495 [CrossRef Medline](#)
- Ishii, K. A., Fumoto, T., Iwai, K., Takeshita, S., Ito, M., Shimohata, N., Aburatani, H., Taketani, S., Lelliott, C. J., Vidal-Puig, A., and Ikeda, K. (2009) Coordination of PGC-1 β and iron uptake in mitochondrial biogenesis and osteoclast activation. *Nat. Med.* **15**, 259–266 [CrossRef Medline](#)
- Jin, Z., Wei, W., Yang, M., Du, Y., and Wan, Y. (2014) Mitochondrial complex I activity suppresses inflammation and enhances bone resorption by shifting macrophage-osteoclast polarization. *Cell Metab.* **20**, 483–498 [CrossRef Medline](#)
- Wei, W., Wang, X., Yang, M., Smith, L. C., Dechow, P. C., Sonoda, J., Evans, R. M., and Wan, Y. (2010) PGC1 β mediates PPAR γ activation of osteoclastogenesis and rosiglitazone-induced bone loss. *Cell Metab.* **11**, 503–516 [CrossRef Medline](#)
- Nunnari, J., and Suomalainen, A. (2012) Mitochondria: in sickness and in health. *Cell* **148**, 1145–1159 [CrossRef Medline](#)
- Finkel, T. (2011) Signal transduction by reactive oxygen species. *J. Cell Biol.* **194**, 7–15 [CrossRef Medline](#)
- Murphy, M. P., Holmgren, A., Larsson, N. G., Halliwell, B., Chang, C. J., Kalyanaraman, B., Rhee, S. G., Thornalley, P. J., Partridge, L., Gems, D., Nyström, T., Belousov, V., Schumacker, P. T., and Winterbourn, C. C. (2011) Unraveling the biological roles of reactive oxygen species. *Cell Metab.* **13**, 361–366 [CrossRef Medline](#)
- Garrett, I. R., Boyce, B. F., Oreffo, R. O., Bonewald, L., Poser, J., and Mundy, G. R. (1990) Oxygen-derived free radicals stimulate osteoclastic bone resorption in rodent bone *in vitro* and *in vivo*. *J. Clin. Invest.* **85**, 632–639 [CrossRef Medline](#)
- Lean, J. M., Jagger, C. J., Kirstein, B., Fuller, K., and Chambers, T. J. (2005) Hydrogen peroxide is essential for estrogen-deficiency bone loss and osteoclast formation. *Endocrinology* **146**, 728–735 [CrossRef Medline](#)
- Bartell, S. M., Kim, H. N., Ambrogini, E., Han, L., Iyer, S., Serra Ucer, S., Rabinovitch, P., Jilka, R. L., Weinstein, R. S., Zhao, H., O'Brien, C. A., Manolagas, S. C., and Almeida, M. (2014) FoxO proteins restrain osteoclastogenesis and bone resorption by attenuating H₂O₂ accumulation. *Nat. Commun.* **5**, 3773 [Medline](#)
- Kanzaki, H., Shinohara, F., Kajiya, M., and Kodama, T. (2013) The Keap1/Nrf2 protein axis plays a role in osteoclast differentiation by regulating intracellular reactive oxygen species signaling. *J. Biol. Chem.* **288**, 23009–23020 [CrossRef Medline](#)
- Lean, J. M., Davies, J. T., Fuller, K., Jagger, C. J., Kirstein, B., Partington, G. A., Urry, Z. L., and Chambers, T. J. (2003) A crucial role for thiol antioxidants in estrogen-deficiency bone loss. *J. Clin. Invest.* **112**, 915–923 [CrossRef Medline](#)
- Ha, H., Kwak, H. B., Lee, S. W., Jin, H. M., Kim, H. M., Kim, H. H., and Lee, Z. H. (2004) Reactive oxygen species mediate RANK signaling in osteoclasts. *Exp. Cell Res.* **301**, 119–127 [CrossRef Medline](#)
- Kim, M. S., Yang, Y. M., Son, A., Tian, Y. S., Lee, S. I., Kang, S. W., Muallem, S., and Shin, D. M. (2010) RANKL-mediated reactive oxygen species pathway that induces long lasting Ca²⁺ oscillations essential for osteoclastogenesis. *J. Biol. Chem.* **285**, 6913–6921 [CrossRef Medline](#)
- Lee, N. K., Choi, Y. G., Baik, J. Y., Han, S. Y., Jeong, D. W., Bae, Y. S., Kim, N., and Lee, S. Y. (2005) A crucial role for reactive oxygen species in RANKL-induced osteoclast differentiation. *Blood* **106**, 852–859 [CrossRef Medline](#)
- Goettsch, C., Babelova, A., Trummer, O., Erben, R. G., Rauner, M., Rammelt, S., Weissmann, N., Weinberger, V., Benkhoff, S., Kampschulte, M., Obermayer-Pietsch, B., Hofbauer, L. C., Brandes, R. P., and Schröder, K. (2013) NADPH oxidase 4 limits bone mass by promoting osteoclastogenesis. *J. Clin. Invest.* **123**, 4731–4738 [CrossRef Medline](#)
- Kang, I. S., and Kim, C. (2016) NADPH oxidase gp91phox contributes to RANKL-induced osteoclast differentiation by upregulating NFATc1. *Sci. Rep.* **6**, 38014 [CrossRef Medline](#)

30. Kim, H., Kim, T., Jeong, B. C., Cho, I. T., Han, D., Takegahara, N., Negishi-Koga, T., Takayanagi, H., Lee, J. H., Sul, J. Y., Prasad, V., Lee, S. H., and Choi, Y. (2013) Tmem64 modulates calcium signaling during RANKL-mediated osteoclast differentiation. *Cell Metab.* **17**, 249–260 [CrossRef Medline](#)
31. Kim, H., Lee, Y. D., Kim, H. J., Lee, Z. H., and Kim, H. H. (2017) SOD2 and Sirt3 control osteoclastogenesis by regulating mitochondrial ROS. *J. Bone Miner. Res.* **32**, 397–406 [Medline](#)
32. Srinivasan, S., Koenigstein, A., Joseph, J., Sun, L., Kalyanaraman, B., Zaidi, M., and Avadhani, N. G. (2010) Role of mitochondrial reactive oxygen species in osteoclast differentiation. *Ann. N.Y. Acad. Sci.* **1192**, 245–252 [CrossRef Medline](#)
33. Andrews, N. C. (2000) Iron homeostasis: insights from genetics and animal models. *Nat. Rev. Genet.* **1**, 208–217 [CrossRef Medline](#)
34. Xu, W., Barrientos, T., and Andrews, N. C. (2013) Iron and copper in mitochondrial diseases. *Cell Metab.* **17**, 319–328 [CrossRef Medline](#)
35. Lawen, A., and Lane, D. J. (2013) Mammalian iron homeostasis in health and disease: uptake, storage, transport, and molecular mechanisms of action. *Antioxid. Redox Signal.* **18**, 2473–2507 [CrossRef Medline](#)
36. Pantopoulos, K., Porwal, S. K., Tartakoff, A., and Devireddy, L. (2012) Mechanisms of mammalian iron homeostasis. *Biochemistry* **51**, 5705–5724 [CrossRef Medline](#)
37. Hentze, M. W., Muckenthaler, M. U., Galy, B., and Camaschella, C. (2010) Two to tango: regulation of mammalian iron metabolism. *Cell* **142**, 24–38 [CrossRef Medline](#)
38. Ward, D. M., and Kaplan, J. (2012) Ferroportin-mediated iron transport: expression and regulation. *Biochim. Biophys. Acta* **1823**, 1426–1433 [CrossRef Medline](#)
39. Fernandes, A., Preza, G. C., Phung, Y., De Domenico, I., Kaplan, J., Ganz, T., and Nemeth, E. (2009) The molecular basis of hepcidin-resistant hereditary hemochromatosis. *Blood* **114**, 437–443 [CrossRef Medline](#)
40. Montosi, G., Donovan, A., Totaro, A., Garuti, C., Pignatti, E., Cassanelli, S., Trenor, C. C., Gasparini, P., Andrews, N. C., and Pietrangelo, A. (2001) Autosomal-dominant hemochromatosis is associated with a mutation in the ferroportin (SLC11A3) gene. *J. Clin. Invest.* **108**, 619–623 [CrossRef Medline](#)
41. Njajou, O. T., Vaessen, N., Joosse, M., Berghuis, B., van Dongen, J. W., Breuning, M. H., Snijders, P. J., Rutten, W. P., Sandkuijl, L. A., Oostra, B. A., van Duijn, C. M., and Heutink, P. (2001) A mutation in SLC11A3 is associated with autosomal dominant hemochromatosis. *Nat. Genet.* **28**, 213–214 [CrossRef Medline](#)
42. Donovan, A., Lima, C. A., Pinkus, J. L., Pinkus, G. S., Zon, L. I., Robine, S., and Andrews, N. C. (2005) The iron exporter ferroportin/Slc40a1 is essential for iron homeostasis. *Cell Metab.* **1**, 191–200 [CrossRef Medline](#)
43. Zhang, Z., Zhang, F., An, P., Guo, X., Shen, Y., Tao, Y., Wu, Q., Zhang, Y., Yu, Y., Ning, B., Nie, G., Knutson, M. D., Anderson, G. J., and Wang, F. (2011) Ferroportin1 deficiency in mouse macrophages impairs iron homeostasis and inflammatory responses. *Blood* **118**, 1912–1922 [CrossRef Medline](#)
44. Gu, Z., Wang, H., Xia, J., Yang, Y., Jin, Z., Xu, H., Shi, J., De Domenico, I., Tricot, G., and Zhan, F. (2015) Decreased ferroportin promotes myeloma cell growth and osteoclast differentiation. *Cancer Res.* **75**, 2211–2221 [CrossRef Medline](#)
45. Almeida, M., Han, L., Martin-Millan, M., O'Brien, C. A., and Manolagas, S. C. (2007) Oxidative stress antagonizes Wnt signaling in osteoblast precursors by diverting β -catenin from T cell factor to forkhead box O-mediated transcription. *J. Biol. Chem.* **282**, 27298–27305 [CrossRef Medline](#)
46. Dede, A. D., Trovas, G., Chronopoulos, E., Triantafyllopoulos, I. K., Dontas, I., Papaioannou, N., and Tournis, S. (2016) Thalassemia-associated osteoporosis: a systematic review on treatment and brief overview of the disease. *Osteoporos. Int.* **27**, 3409–3425 [CrossRef Medline](#)
47. Guggenbuhl, P., Brissot, P., and Loréal, O. (2011) Miscellaneous non-inflammatory musculoskeletal conditions. Haemochromatosis: the bone and the joint. *Best Pract. Res. Clin. Rheumatol.* **25**, 649–664 [CrossRef Medline](#)
48. Fung, E. B., Harmatz, P. R., Milet, M., Coates, T. D., Thompson, A. A., Ranalli, M., Mignaca, R., Scher, C., Giardina, P., Robertson, S., Neumayr, L., Vichinsky, E. P., and Multi-Center Iron Overload Study Group. (2008) Fracture prevalence and relationship to endocrinopathy in iron overloaded patients with sickle cell disease and thalassemia. *Bone* **43**, 162–168 [CrossRef Medline](#)
49. Guggenbuhl, P., Deugnier, Y., Boisdet, J. F., Rolland, Y., Perdriger, A., Pawlotsky, Y., and Chales, G. (2005) Bone mineral density in men with genetic hemochromatosis and HFE gene mutation. *Osteoporos. Int.* **16**, 1809–1814 [CrossRef Medline](#)
50. Vogiatzi, M. G., Macklin, E. A., Fung, E. B., Cheung, A. M., Vichinsky, E., Olivieri, N., Kirby, M., Kwiatkowski, J. L., Cunningham, M., Holm, I. A., Lane, J., Schneider, R., Fleisher, M., Grady, R. W., Peterson, C. C., Giardina, P. J., and Thalassemia Clinical Research Network. (2009) Bone disease in thalassemia: a frequent and still unresolved problem. *J. Bone Miner. Res.* **24**, 543–557 [CrossRef Medline](#)
51. Vogiatzi, M. G., Macklin, E. A., Fung, E. B., Vichinsky, E., Olivieri, N., Kwiatkowski, J., Cohen, A., Neufeld, E., and Giardina, P. J. (2006) Prevalence of fractures among the thalassemia syndromes in North America. *Bone* **38**, 571–575 [CrossRef Medline](#)
52. Voskaridou, E., Kyrtonis, M. C., Terpos, E., Skordili, M., Theodoropoulos, I., Bergele, A., Diamanti, E., Kalovidouris, A., Loutradi, A., and Loukopoulos, D. (2001) Bone resorption is increased in young adults with thalassaemia major. *Br. J. Haematol.* **112**, 36–41 [CrossRef Medline](#)
53. Mahachoklertwattana, P., Sirikulchayanonta, V., Chuansumrit, A., Karnsombat, P., Choubtum, L., Sriphrapradang, A., Domrongkitchaiporn, S., Sirisriro, R., and Rajatanavin, R. (2003) Bone histomorphometry in children and adolescents with β -thalassaemia disease: iron-associated focal osteomalacia. *J. Clin. Endocrinol. Metab.* **88**, 3966–3972 [CrossRef Medline](#)
54. Tsay, J., Yang, Z., Ross, F. P., Cunningham-Rundles, S., Lin, H., Coleman, R., Mayer-Kuckuk, P., Doty, S. B., Grady, R. W., Giardina, P. J., Boskey, A. L., and Vogiatzi, M. G. (2010) Bone loss caused by iron overload in a murine model: importance of oxidative stress. *Blood* **116**, 2582–2589 [CrossRef Medline](#)
55. Xiao, W., Beibei, F., Guangsi, S., Yu, J., Wen, Z., Xi, H., and Youjia, X. (2015) Iron overload increases osteoclastogenesis and aggravates the effects of ovariectomy on bone mass. *J. Endocrinol.* **226**, 121–134 [CrossRef Medline](#)
56. Guo, J. P., Pan, J. X., Xiong, L., Xia, W. F., Cui, S., and Xiong, W. C. (2015) Iron chelation inhibits osteoclastic differentiation *in vitro* and in Tg2576 mouse model of Alzheimer's disease. *PLoS One* **10**, e0139395 [CrossRef Medline](#)
57. Clausen, B. E., Burkhardt, C., Reith, W., Renkawitz, R., and Förster, I. (1999) Conditional gene targeting in macrophages and granulocytes using LysMcre mice. *Transgenic Res.* **8**, 265–277 [CrossRef Medline](#)
58. Nakamura, T., Imai, Y., Matsumoto, T., Sato, S., Takeuchi, K., Igarashi, K., Harada, Y., Azuma, Y., Krust, A., Yamamoto, Y., Nishina, H., Takeda, S., Takayanagi, H., Metzger, D., Kanno, J., et al. (2007) Estrogen prevents bone loss via estrogen receptor α and induction of Fas ligand in osteoclasts. *Cell* **130**, 811–823 [CrossRef Medline](#)
59. Rissanen, J. P., Suominen, M. I., Peng, Z., and Halleen, J. M. (2008) Secreted tartrate-resistant acid phosphatase 5b is a Marker of osteoclast number in human osteoclast cultures and the rat ovariectomy model. *Calcif. Tissue Int.* **82**, 108–115 [CrossRef Medline](#)
60. Ito, Y., Teitelbaum, S. L., Zou, W., Zheng, Y., Johnson, J. F., Chappel, J., Ross, F. P., and Zhao, H. (2010) Cdc42 regulates bone modeling and remodeling in mice by modulating RANKL/M-CSF signaling and osteoclast polarization. *J. Clin. Invest.* **120**, 1981–1993 [CrossRef Medline](#)
61. Zhou, P., Kitaura, H., Teitelbaum, S. L., Krystal, G., Ross, F. P., and Takeshita, S. (2006) SHIP1 negatively regulates proliferation of osteoclast precursors via Akt-dependent alterations in D-type cyclins and p27. *J. Immunol.* **177**, 8777–8784 [CrossRef Medline](#)
62. Lee, J. M., Park, H., Noh, A. L., Kang, J. H., Chen, L., Zheng, T., Lee, J., Ji, S. Y., Jang, C. Y., Shin, C. S., Ha, H., Lee, Z. H., Park, H. Y., Lee, D. S., and Yim, M. (2012) 5-Lipoxygenase mediates RANKL-induced osteoclast formation via the cysteinyl leukotriene receptor 1. *J. Immunol.* **189**, 5284–5292 [CrossRef Medline](#)
63. Zwerina, J., Tzima, S., Hayer, S., Redlich, K., Hoffmann, O., Hanslik-Schnabel, B., Smolen, J. S., Kollias, G., and Schett, G. (2005) Heme oxyge-

Ferroportin and osteoclast formation

- nase 1 (HO-1) regulates osteoclastogenesis and bone resorption. *FASEB J.* **19**, 2011–2013 [CrossRef Medline](#)
64. Almeida, A., and Roberts, I. (2005) Bone involvement in sickle cell disease. *Br. J. Haematol.* **129**, 482–490 [CrossRef Medline](#)
65. Jeney, V. (2017) Clinical impact and cellular mechanisms of iron overload-associated bone loss. *Front. Pharmacol.* **8**, 77 [Medline](#)
66. Beaumont, C., and Delaby, C. (2009) Recycling iron in normal and pathological states. *Semin. Hematol.* **46**, 328–338 [CrossRef Medline](#)
67. Guggenbuhl, P., Fergelot, P., Doyard, M., Libouban, H., Roth, M. P., Gallois, Y., Chalès, G., Loréal, O., and Chappard, D. (2011) Bone status in a mouse model of genetic hemochromatosis. *Osteoporos. Int.* **22**, 2313–2319 [CrossRef Medline](#)
68. Sun, L., Guo, W., Yin, C., Zhang, S., Qu, G., Hou, Y., Rong, H., Ji, H., and Liu, S. (2014) Hepcidin deficiency undermines bone load-bearing capacity through inducing iron overload. *Gene* **543**, 161–165 [CrossRef Medline](#)
69. Thongchote, K., Svasti, S., Teerapornpuntakit, J., Suntornsaratoon, P., Krishnamra, N., and Charoenphandhu, N. (2015) Bone microstructural defects and osteopenia in hemizygous β IVSII-654 knockin thalassemic mice: sex-dependent changes in bone density and osteoclast function. *Am. J. Physiol. Endocrinol. Metab.* **309**, E936–E948 [CrossRef Medline](#)
70. Jia, P., Xu, Y. J., Zhang, Z. L., Li, K., Li, B., Zhang, W., and Yang, H. (2012) Ferric ion could facilitate osteoclast differentiation and bone resorption through the production of reactive oxygen species. *J. Orthop. Res.* **30**, 1843–1852 [CrossRef Medline](#)
71. Crownover, B. K., and Covey, C. J. (2013) Hereditary hemochromatosis. *Am. Fam. Physician* **87**, 183–190 [Medline](#)
72. Dhindsa, S., Ghanim, H., Batra, M., Kuhadiya, N. D., Abuaysheh, S., Green, K., Makdissi, A., Chaudhuri, A., and Dandona, P. (2016) Effect of testosterone on hepcidin, ferroportin, ferritin and iron binding capacity in patients with hypogonadotropic hypogonadism and type 2 diabetes. *Clin. Endocrinol.* **85**, 772–780 [CrossRef](#)
73. Hou, Y., Zhang, S., Wang, L., Li, J., Qu, G., He, J., Rong, H., Ji, H., and Liu, S. (2012) Estrogen regulates iron homeostasis through governing hepatic hepcidin expression via an estrogen response element. *Gene* **511**, 398–403 [CrossRef Medline](#)
74. Yang, Q., Jian, J., Katz, S., Abramson, S. B., and Huang, X. (2012) 17 β -Estradiol inhibits iron hormone hepcidin through an estrogen responsive element half-site. *Endocrinology* **153**, 3170–3178 [CrossRef Medline](#)
75. Qian, Y., Yin, C., Chen, Y., Zhang, S., Jiang, L., Wang, F., Zhao, M., and Liu, S. (2015) Estrogen contributes to regulating iron metabolism through governing ferroportin signaling via an estrogen response element. *Cell Signal.* **27**, 934–942 [CrossRef Medline](#)
76. Milman, N., Kirchhoff, M., and Jørgensen, T. (1992) Iron status markers, serum ferritin and hemoglobin in 1359 Danish women in relation to menstruation, hormonal contraception, parity, and postmenopausal hormone treatment. *Ann. Hematol.* **65**, 96–102 [CrossRef Medline](#)
77. Zacharski, L. R., Ornstein, D. L., Woloshin, S., and Schwartz, L. M. (2000) Association of age, sex, and race with body iron stores in adults: analysis of NHANES III data. *Am. Heart J.* **140**, 98–104 [CrossRef Medline](#)
78. Zhang, L. L., Jiang, X. F., Ai, H. Z., Jin, Z. D., Xu, J. X., Wang, B., Xu, W., Xie, Z. G., Zhou, H. B., Dong, Q. R., and Xu, Y. J. (2013) Relationship of iron overload to bone mass density and bone turnover in postmenopausal women with fragility fractures of the hip. *Zhonghua wai ke za zhi* **51**, 518–521 [Medline](#)
79. Kim, B. J., Lee, S. H., Koh, J. M., and Kim, G. S. (2013) The association between higher serum ferritin level and lower bone mineral density is prominent in women ≥ 45 years of age (KNHANES 2008–2010). *Osteoporos. Int.* **24**, 2627–2637 [CrossRef Medline](#)
80. Kim, B. J., Ahn, S. H., Bae, S. J., Kim, E. H., Lee, S. H., Kim, H. K., Choe, J. W., Koh, J. M., and Kim, G. S. (2012) Iron overload accelerates bone loss in healthy postmenopausal women and middle-aged men: a 3-year retrospective longitudinal study. *J. Bone Miner. Res.* **27**, 2279–2290 [CrossRef Medline](#)
81. Zhao, G. Y., Di, D. H., Wang, B., Huang, X., and Xu, Y. J. (2015) Effects of mouse hepcidin 1 treatment on osteoclast differentiation and intracellular iron concentration. *Inflammation* **38**, 718–727 [CrossRef Medline](#)
82. Xie, W., Lorenz, S., Dolder, S., and Hofstetter, W. (2016) Extracellular iron is a modulator of the differentiation of osteoclast lineage cells. *Calcif. Tissue Int.* **98**, 275–283 [CrossRef Medline](#)
83. Ye, S., Fujiwara, T., Zhou, J., Varughese, K. I., and Zhao, H. (2016) LIS1 regulates osteoclastogenesis through modulation of M-SCF and RANKL signaling pathways and CDC42. *Int. J. Biol. Sci.* **12**, 1488–1499 [CrossRef Medline](#)
84. Fujiwara, T., Zhou, J., Ye, S., and Zhao, H. (2016) RNA-binding protein Musashi2 induced by RANKL is critical for osteoclast survival. *Cell Death Dis.* **7**, e2300 [CrossRef Medline](#)
85. Takeshita, S., Kaji, K., and Kudo, A. (2000) Identification and characterization of the new osteoclast progenitor with macrophage phenotypes being able to differentiate into mature osteoclasts. *J. Bone Miner. Res.* **15**, 1477–1488 [CrossRef Medline](#)
86. Zhou, J., Ye, S., Fujiwara, T., Manolagas, S. C., and Zhao, H. (2013) Steap4 plays a critical role in osteoclastogenesis *in vitro* by regulating cellular iron/reactive oxygen species (ROS) levels and cAMP response element-binding protein (CREB) activation. *J. Biol. Chem.* **288**, 30064–30074 [CrossRef Medline](#)
87. Fujiwara, T., Ye, S., Castro-Gomes, T., Winchell, C. G., Andrews, N. W., Voth, D. E., Varughese, K. I., Mackintosh, S. G., Feng, Y., Pavlos, N., Nakamura, T., Manolagas, S. C., and Zhao, H. (2016) PLEKHM1/DEF8/RAB7 complex regulates lysosome positioning and bone homeostasis. *JCI Insight* **1**, e86330 [Medline](#)
88. Zhao, H., and Väänänen, H. K. (2006) Pharmacological sequestration of intracellular cholesterol in late endosomes disrupts ruffled border formation in osteoclasts. *J. Bone Miner. Res.* **21**, 456–465 [Medline](#)
89. Ye, S., Fowler, T. W., Pavlos, N. J., Ng, P. Y., Liang, K., Feng, Y., Zheng, M., Kurten, R., Manolagas, S. C., and Zhao, H. (2011) LIS1 regulates osteoclast formation and function through its interactions with dynein/dynactin and Plekhm1. *PLoS One* **6**, e27285 [CrossRef Medline](#)
90. Garrick, L. M., Gniecko, K., Hoke, J. E., al-Nakeeb, A., Ponka, P., and Garrick, M. D. (1991) Ferric-salicylaldehyde isonicotinoyl hydrazone, a synthetic iron chelate, alleviates defective iron utilization by reticulocytes of the Belgrade rat. *J. Cell. Physiol.* **146**, 460–465 [CrossRef Medline](#)